

GENERAL PHYSICAL PROPERTIES OF *CGRABS* BLAZARS

VAIDEHI S. PALIYA¹, L. MARCOTULLI¹, M. AJELLO¹, M. JOSHI², S. SAHAYANATHAN³, A. R. RAO⁴, AND D. HARTMANN¹

¹Department of Physics and Astronomy, Clemson University, Kinard Lab of Physics, Clemson, SC 29634-0978, USA

²Institute for Astrophysical Research, Boston University, 725 Commonwealth Avenue, Boston, MA 02215, USA

³Astrophysical Sciences Division, Bhabha Atomic Research Centre, Mumbai-400085, India

and

⁴Department of Astronomy and Astrophysics, Tata Institute of Fundamental Research, Homi Bhabha Road, Mumbai, India

ABSTRACT

We present the results of a multi-frequency, time-averaged analysis of blazars included in the Candidate Gamma-ray Blazar Survey catalog. Our sample consists of 324 γ -ray detected (γ -ray loud) and 191 non γ -ray detected (γ -ray quiet) blazars, and we consider all the data up to 2016 April 1. We find that both the γ -ray loud and the γ -ray quiet blazar populations occupy similar regions in the *WISE* color-color diagram, and in the radio and X-ray bands γ -ray loud sources are brighter. A simple one-zone synchrotron inverse-Compton emission model is applied to derive the physical properties of both populations. We find that the central black hole mass and the accretion disk luminosity (L_{disk}) computed from the modeling of the optical-UV emission with a Shakura-Sunyaev disk reasonably matches with that estimated from the optical spectroscopic emission-line information. A significantly larger Doppler boosting in the γ -ray loud blazars is noted, and their jets are more radiatively efficient. On the other hand, the γ -ray quiet objects are more MeV-peaked, thus could be potential targets for next-generation MeV missions. Our results confirm the earlier findings about the accretion-jet connection in blazars; however, many of the γ -ray quiet blazars tend to deviate from the recent claim that the jet power exceeds L_{disk} in blazars. A broadband study, considering a larger set of γ -ray quiet objects and also including BL Lacs, will be needed to confirm/reject this hypothesis and also to verify the evolution of the powerful high-redshift blazars into their low-power nearby counterparts.

Keywords: galaxies: active — gamma-ray: galaxies— galaxies: jets— galaxies: high-redshift— quasars: general

1. INTRODUCTION

Blazars are radio-loud (RL) active galactic nuclei (AGN) that are known to host powerful relativistic jets closely aligned to the line of sight to the observer (e.g., Urry & Padovani 1995). Blazars are known to emit radiation over the entire electromagnetic spectrum, from low-energy radio waves to very-high-energy γ -rays, and they also exhibit flux and polarization variations (Stalin et al. 2002; Sagar et al. 2004; Jorstad et al. 2010; Aleksić et al. 2011; Bachev et al. 2012; Paliya et al. 2015; Marchesini et al. 2016). All these effects are believed to arise from the Doppler boosting that occurs due to the peculiar orientation of the jet (viewing angle $\theta_v < 1/\Gamma$; where Γ is the bulk Lorentz factor of the jet). Accordingly, for each observed blazar with a known Γ there

exist $2\Gamma^2$ intrinsically similar sources with their jets pointed in other directions.

Based on the equivalent width (EW) of the optical emission lines, blazars are classified as flat spectrum radio quasars (FSRQs) and BL Lac objects, with FSRQs exhibiting broad emission lines ($\text{EW} > 5\text{\AA}$). The observation of strong emission lines from FSRQs indicates the presence of a luminous broad line region (BLR), which in turn suggests a high and efficient accretion process that illuminates the BLR (e.g., Sbarrato et al. 2012). In fact, the infrared-to-ultraviolet (IR to UV) spectrum of many FSRQs is found to be dominated by the thermal emission from the accretion disk (e.g., Ghisellini et al. 2010). The presence/absence of narrow emission lines in the optical spectrum of BL Lac objects, on the other hand, indicates a relatively low and inefficient accretion and/or the dominance of the non-thermal synchrotron radiation originating from the plasma moving along the relativistic jet.

The radio to γ -ray spectral energy distribution (SED) of

blazars exhibits a characteristic double hump structure. The low-energy peak lies at radio to optical-UV or X-ray frequencies and is attributed to synchrotron emission, whereas the origin of the high-energy peak is often associated to the inverse Compton (IC) scattering off low-energy photons by the energetic electrons present in the jet. When the low-energy target photons are provided by synchrotron emission, the IC mechanism is called synchrotron self Compton (SSC; e.g., Marscher & Gear 1985). This, along with the synchrotron process, is found to satisfactorily explain the broadband SEDs of BL Lac objects (e.g., Tavecchio et al. 2010; Yan et al. 2014). On the other hand, the high-energy γ -ray emission from powerful FSRQs is conventionally explained by the IC process with low-energy photons originating outside the jet (External Compton or EC; e.g., Begelman & Sikora 1987). In this case, the reservoirs of seed photons for IC mechanism could be the accretion disk (Dermer & Schlickeiser 1993), the BLR (Sikora et al. 1994), and/or the dusty torus (Błażejowski et al. 2000). The SED of blazars is also successfully reproduced by hadronic processes (e.g., Mücke et al. 2000), though the resulting parameters (e.g., magnetic field) are found to be quite extreme (e.g., Abdo et al. 2011).

It is well known since the Energetic Gamma Ray Experiment Telescope (Thompson et al. 1993) era that the high-energy γ -ray extragalactic sky is dominated by blazars (Hartman et al. 1999). This has later been confirmed with the advent of the Large Area Telescope onboard *Fermi Gamma-ray Space Telescope* (*Fermi*-LAT; Atwood et al. 2009). In fact, *Fermi*-LAT detected more than a thousand blazars in its first four years of operation (Ackermann et al. 2015). The availability of good quality *Fermi*-LAT data, complemented by the lower-frequency monitoring from various observing facilities¹, has allowed population studies of blazars (see, e.g., Ghisellini et al. 2009, 2010; Tavecchio et al. 2010; Meyer et al. 2011; Ajello et al. 2012; Giommi et al. 2012b; Finke 2013; Ajello et al. 2014; Ghisellini et al. 2014; Kang et al. 2014; Zhang et al. 2014; Chen et al. 2015; Ghisellini & Tavecchio 2015; Fan et al. 2016; Krauß et al. 2016; Mao et al. 2016; Ghisellini et al. 2017).

Though *Fermi*-LAT has observed a significant γ -ray emission from a large number of blazars, an even larger number of such sources is yet to be detected in the γ -ray band (e.g., Massaro et al. 2015). Various explanations have been proposed to explain this, such as the differences in the Doppler boosting, apparent jet speed, apparent opening angle, very long baseline interferometry core flux densities, and brightness temperatures (Pushkarev et al. 2009; Lister et al. 2015).

Motivated by the availability of good quality multi-wavelength (MW) data set for a large number of blazars, we

Table 1. The CGRaBS sample studied in this work. Apart from them, we also include four CGRaBS blazars that were recently reported as γ -ray emitting source in literature. See the text for details.

γ -ray loud		
Catalog	FSRQs	BL Lacs
3FGL	235	75
2FGL	8	0
1FGL	2	0
γ -ray quiet		
Catalog	FSRQs	BL Lacs
CGRaBS	185	6

systematically study their broadband properties using both observational and theoretical SED modeling approaches. Our primary goal is to investigate the fundamental properties of blazars such as the accretion-jet connection, the cosmological evolution of relativistic jets and also the differences in the physical characteristics of the known γ -ray sources and non γ -ray emitters. Compared to earlier studies, we focus on the observational results and then interpret them using a leptonic emission model. Here we present the results of our study on the blazars included in the Candidate Gamma-ray Blazars Survey catalog (CGRaBS; Healey et al. 2008). Ours is probably the largest sample of blazars on which a physical SED model is applied. In Section 2 we describe the steps adopted to select the objects, and in Section 3 the details of the data reduction procedures are given. The observational results are presented in Section 4. We briefly describe the adopted one-zone leptonic emission model in Section 5 and present the results associated with the SED modeling in Section 6. We discuss our findings in Section 7 and summarize in Section 8.

We adopt a flat cosmology with $H_0 = 67.8 \text{ km s}^{-1} \text{ Mpc}^{-1}$ and $\Omega_M = 0.308$ (Planck Collaboration et al. 2016).

2. THE SAMPLE

CGRaBS is a flux-limited (8.4 GHz flux density $> 65 \text{ mJy}$, see also, Healey et al. 2007) catalog of 1625 high-latitude ($|b| > 10^\circ$), flat radio spectrum objects prepared to serve for the MW followup of likely γ -ray emitting AGNs (Healey et al. 2008). To determine the γ -ray detected CGRaBS blazars, we cross-match CGRaBS with all of the *Fermi*-LAT catalogs² (3FGL, 2FGL, 1FGL, and 0FGL, sequentially; Acero et al. 2015; Nolan et al. 2012; Abdo et al. 2010, 2009). This is done by searching for a CGRaBS counterpart of the γ -ray source within its 95% positional uncertainty. We consider a source to be γ -ray detected if it is in-

¹ <https://fermi.gsfc.nasa.gov/ssc/observations/multi/programs.html>

² The motivation behind cross-matching CGRaBS with all of the *Fermi*-LAT catalogs is to take into account the possibility that an object might have appeared in earlier catalogs but was left out in later ones, probably due to the detection significance of the source falling below the threshold.

cluded in any of the *Fermi*-LAT catalogs. We find a total of 467 matches and 1178 remain as no-LAT detected. Further, we look into the HEASARC archive for the availability of MW data, particularly X-rays. In our final sample, we keep only sources that have existing MW data set and have redshift information either given in *Fermi*-LAT AGN catalogs or in CGRaBS. This exercise has led to the inclusion of 515 CGRaBS sources comprising 324 γ -ray detected (or γ -ray loud) blazars and 191 non γ -ray detected (hereafter γ -ray quiet) objects. Table 1 presents the breakdown of sources by type for the entire sample. We also consider four CGRaBS blazars that were recently reported as new γ -ray emitters. These include J0225+1846³ (Paliya et al. 2016), J0646+4451 and J2129–1538 (Ackermann et al. 2017) and J1829–5813 (Buson 2014). Moreover, we keep the FSRQ/BL Lac distinction as given in *Fermi*-LAT catalogs or in CGRaBS⁴. Since there are only a few BL Lac objects present in our sample ($\sim 15\%$), we refrain from performing a detailed comparison of their physical properties with FSRQs and defer it to a future publication where we will consider all *Fermi*-LAT detected blazars, including those FSRQs and BL Lac objects that are not present in this work (Paliya et al., in preparation). Instead, here we focus on comparing the MW properties of the γ -ray loud and the γ -ray quiet CGRaBS sources.

Our results are based on the time-averaged study of CGRaBS sources, as we have considered all of the available MW data (up to 2016 April 1) without producing for each source multiple SEDs with only contemporaneous data. Blazars are known to show fast variability; however, due to our very large sample such detailed analysis was not feasible. The non-simultaneity could affect the parameters of the individual objects; however, in an overall statistical sense the derived distributions of the results are reliable. We assume that the averaged data represent a typical activity state of the source. This assumption may not be valid for any individual blazar, but it is a reasonable choice when studying hundreds of objects. The motivation is to characterize the population as a whole. Our approach is similar to that adopted in Ghisellini & Tavecchio (2015), although we also reduce the MW data to understand the observational properties of CGRaBS quasars, and we update the γ -ray results using the latest advancements in the *Fermi*-LAT data, particularly the release of the Pass 8 dataset (Atwood et al. 2013). Furthermore, our sample size is significantly larger and consists of both γ -ray loud and γ -ray quiet blazars, whereas Ghisellini & Tavecchio (2015) have focused solely on γ -ray loud objects.

3. DATA REDUCTION

3.1. *Fermi*-LAT

We consider the *Fermi*-LAT Pass 8 source class photons collected for the period 2008 August 5 to 2016 April 1 (~ 92 months) for all 515 blazars studied in this work. We follow the standard data reduction procedure⁵, but with a few modifications (see also, Ackermann et al. 2017). A sky model is defined considering all γ -ray sources included in 3FGL (Acero et al. 2015) lying within a region of interest (ROI) of 15° radius centered on the target quasar. The isotropic and Galactic diffuse emission models (Acero et al. 2016) are also considered. We perform a binned likelihood analysis to derive the best optimized spectral parameters of all of the sources and power-law normalization factors of the diffuse background models. The significance of the source detection is computed by means of the maximum likelihood test statistic $TS = 2\Delta \log \mathcal{L}$, where \mathcal{L} denotes the likelihood function, between models with and without a point object at the position of the source of interest. The spectral models of all of the *Fermi*-LAT detected blazars are the same as those considered in the LAT catalogs, whereas for the remaining γ -ray quiet sources we adopt a simple power-law model to compute the upper limits.

We use a minimum energy of 60 MeV and set the energy upper limit (E_{\max}) to 300 GeV. To account for the poorer energy resolution of the *Fermi*-LAT at lower energies we enable the energy dispersion correction for all of the objects except the background diffuse models. Moreover, Pass 8 introduces the classification of photons by point-spread-function (PSF) type, sub-classified into four quartiles by quality of directional reconstruction, with the lowest (PSF0) and the highest (PSF3) quartiles having the worst and the best, respectively, angular reconstruction. We perform a component-wise analysis for each PSF and finally perform a joint fitting using the SUMMED likelihood method of the Science Tools⁶.

In order to search for faint γ -ray emitters that are present in the data but not in the 3FGL catalog, we adopt an iterative approach. This step is necessary to update the background models in order to derive the accurate spectral parameters for the sources of interest. We generate a residual TS map for each ROI and scan it for unmodeled excess emissions ($TS \geq 25$). Once found, the locations of such unmodeled objects are optimized and inserted in the model file with a power-law spectrum. We repeat this procedure until the TS map stops showing any excess emission.

For γ -ray quiet blazars, we calculate the 3σ *Fermi*-LAT flux sensitivity limit in the direction of the source, for the period covered in the analysis and assuming a photon index of 2.4. For all sources, flux upper limits are derived at 95% confidence for energy bins with $TS < 9$ while generat-

³ We do not use the prefix CGRABS for the sake of clarity.

⁴ If a source is classified as a FSRQ in the *Fermi*-LAT catalog and as a BL Lac in CGRaBS, we consider it as a FSRQ. This is because the *Fermi*-LAT catalogs are updated with more recent results. However, for γ -ray quiet sources we follow the CGRaBS classification.

⁵ <http://fermi.gsfc.nasa.gov/ssc/data/analysis/documentation/>

⁶ <http://fermi.gsfc.nasa.gov/ssc/data/analysis/software/>

ing γ -ray spectra of the sources. All errors associated with the *Fermi*-LAT data analysis are 1σ statistical uncertainties, unless specified. The entire data analysis is performed using the publicly available python package *fermiPy* (Wood et al. 2017).

3.2. *Swift*

We use all of the data from the three instruments onboard the *Swift* satellite (Gehrels et al. 2004): the Burst Alert Telescope (BAT, 15–150 keV; Barthelmy et al. 2005), the X-Ray Telescope (XRT, 0.3–10 keV; Burrows et al. 2005), and the Ultraviolet Optical Telescope (UVOT Roming et al. 2005), which can observe in six filters, *V*, *B*, *U*, *UVW1*, *UVM2*, and *UVW2*.

We use publicly available 70-month *Swift*-BAT survey (Baumgartner et al. 2013) spectra and the instrument response file to cover the hard X-ray (15–150 keV) part of the SEDs of the blazars included in it.

We generate 0.3–10 keV XRT spectrum using the online tool “*Swift*-XRT data product generator⁷” (Evans et al. 2009). The source spectra are appropriately rebinned (20 or 1 counts per bin, depending on the brightness of the source), and we perform the spectral fitting in XSPEC. The faint sources are fitted with a simple power-law model following the C-statistic (Cash 1979). For the remaining objects we follow a χ^2 fitting procedure. In the χ^2 method, we fit two models, power law and log parabola, and choose the best-fitted model based on the outcome of the *f*-test⁸. We consider the Galactic neutral Hydrogen column densities from Kalberla et al. (2005). The uncertainties are estimated at the 90% confidence level.

We combine UVOT snapshots using the tool *uvotimsum* and extract source magnitudes with *uvotsource*. For the latter, we extract the source counts from a circular region of 5'' radius centered at the quasar. The background is chosen as a circular region of the radius of 30'' from a nearby region free from source contamination. The extracted magnitudes are corrected for the Galactic reddening (Schlafly & Finkbeiner 2011) and converted to energy flux using the conversion factors of Breeveld et al. (2011).

3.3. *XMM-Newton* and *Chandra*

The *XMM-Newton* (Jansen et al. 2001) data (0.3–10 keV) are analyzed using the Science Analysis Software version 15.0.0. The task *eproc* is used to generate EPIC-PN event files. We remove the high flaring background using *evselect*. To extract the source and the background spectra, we define the respective regions as circles of 40'' radius each with the source region being centered at the quasar

⁷ http://www.swift.ac.uk/user_objects/

⁸ We prefer a log-parabola model over the power-law, if the *f*-test probability of null hypothesis is $< 10^{-4}$.

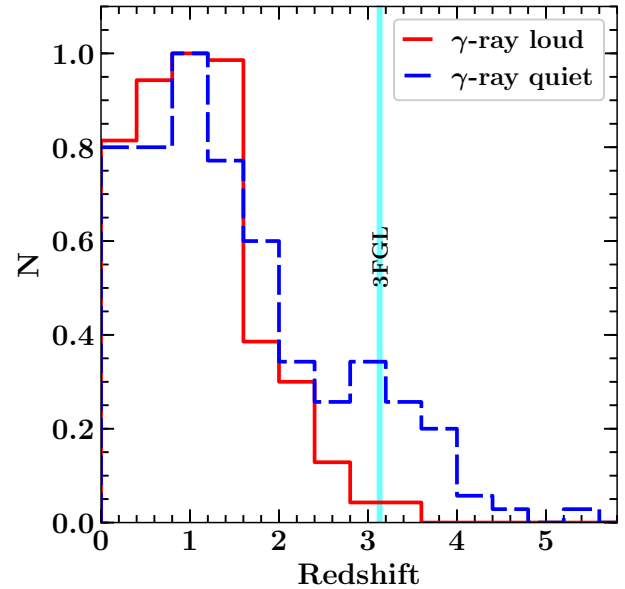


Figure 1. The redshift distribution of γ -ray loud (red solid) and γ -ray quiet (blue dashed) quasars. For an equal comparison, we have normalized the distributions, i.e., the number of the sources at the peak of the distribution has been set equal to unity. The solid cyan line represents the redshift of the most distant known γ -ray emitting blazar in the 3FGL catalog, i.e., $z = 3.1$. New γ -ray loud blazars lie beyond this value (see also, Ackermann et al. 2017).

and the background from the same chip but avoiding contaminating objects. The response files are generated using the tool *rmfgen* and *arfgen*. We bin the spectra using *specgroup* to have a minimum of 20 counts per bin and use XSPEC for spectral fitting.

We reduce the *Chandra* (Weisskopf et al. 2000) Advanced CCD Imaging Spectrometer data (ACIS, 0.3–7 keV) using the package *Chandra Interactive Analysis of Observations* (CIAO, version 4.9) and the associated calibration database (v 4.7.3). The data are first reprocessed with the tool *chandra_repro*. The source and the background spectra are extracted from the cleaned and calibrated event file using the tool *specextract*. A circular region of 3'' radius centered at the source of interest is chosen to extract source counts, and the background is selected as a circle of 10'' radius from a nearby source-free region. The data are binned to have at least 20 or 1 count per bin (depending on the brightness of the source), and we perform the fitting in XSPEC.

4. OBSERVATIONAL CHARACTERISTICS

4.1. Redshift distribution

We show the redshift distribution of both γ -ray loud and γ -ray quiet blazars in Figure 1. The distributions are normalized for an equal comparison. As can be seen, the sample of γ -ray quiet blazars spans a larger redshift range and the most distant γ -ray quiet object has a redshift of 5.47 (J0906+6930; Romani et al. 2004). The relatively low redshifts of γ -ray loud sources could still be due to the relatively high flux

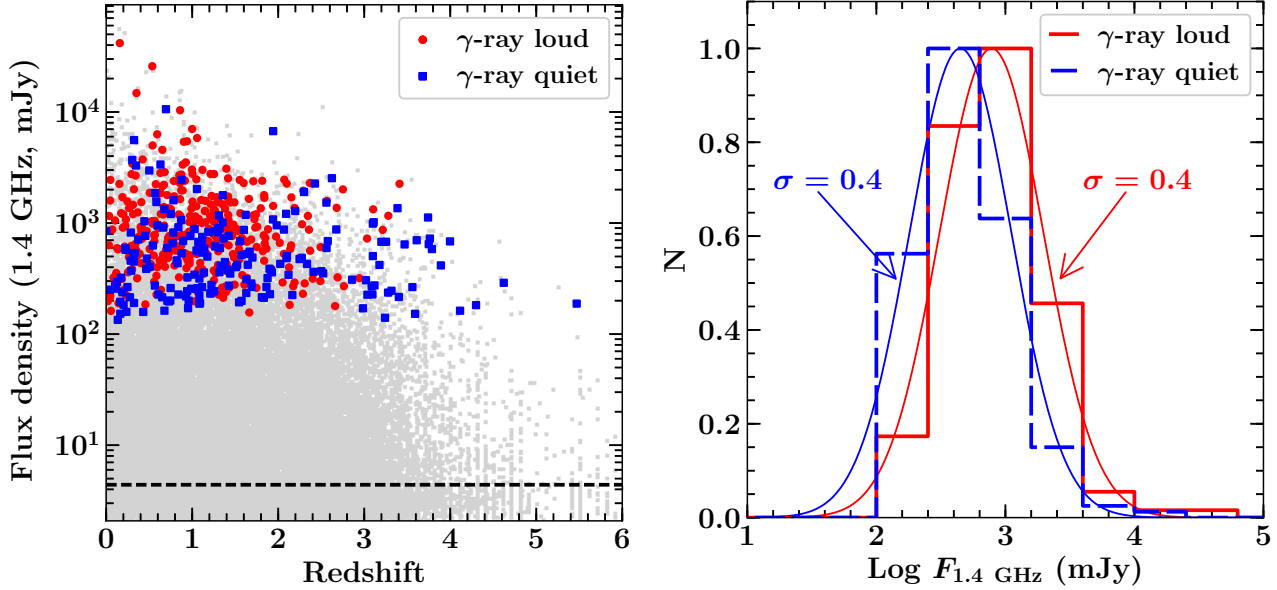


Figure 2. Left: The 1.4 GHz flux density of γ -ray loud (red) and γ -ray quiet (blue) blazars as a function of their redshift. The gray data points correspond to the radio flux densities of the sources included in the Million Quasar Catalog (MQC). The horizontal dashed line represent the median flux density of MQC sources. Right: The radio flux density distributions of γ -ray loud and γ -ray quiet sources. The distributions are fitted with a Gaussian function whose width is quoted.

threshold of *Fermi*-LAT. However, it is important to note that there are two sources in our sample, J0646+4451 ($z = 3.41$) and J2129–1538 ($z = 3.28$), from which significant γ -ray emission is detected. Both these objects are located farther away than the most distant blazar reported in 3FGL (3FGL J0540.0–2837, $z = 3.1$). They were recently found by Ackermann et al. (2017) as new γ -ray loud blazars.

4.2. Radio Properties

Both γ -ray loud and γ -ray quiet objects present in our sample are bright radio sources. In the left panel of Figure 2, we compare the 1.4 GHz flux densities ($F_{1.4 \text{ GHz}}$) of our sources with those included in the Million Quasar Catalog (MQC; Flesch 2015)⁹. All CGRaBS sources have $F_{1.4 \text{ GHz}} > 100$ mJy. They are well above the median radio flux density of MQC objects (~ 5 mJy, shown with a black dashed line). Comparing the γ -ray loud and γ -ray quiet sources (the right panel), we find that the γ -ray loud blazars are brighter ($\langle F_{1.4 \text{ GHz}} \rangle = 776$ mJy) than the γ -ray quiet sources ($\langle F_{1.4 \text{ GHz}} \rangle = 447$ mJy). Fitting the shown distributions with a Gaussian function returns an equal dispersion of 0.4 dex.

4.3. WISE IR-colors

⁹ We derive $F_{1.4 \text{ GHz}}$ from $F_{8.4 \text{ GHz}}$ provided in the CGRaBS catalog, assuming $\alpha = 0$ ($F \propto \nu^\alpha$). For MQC objects, we extract $F_{1.4 \text{ GHz}}$ from the NRAO VLA Sky Survey (NVSS; Condon et al. 1998). This is done by searching for the NVSS counterpart of the MQC source within the positional uncertainty reported in the NVSS catalog.

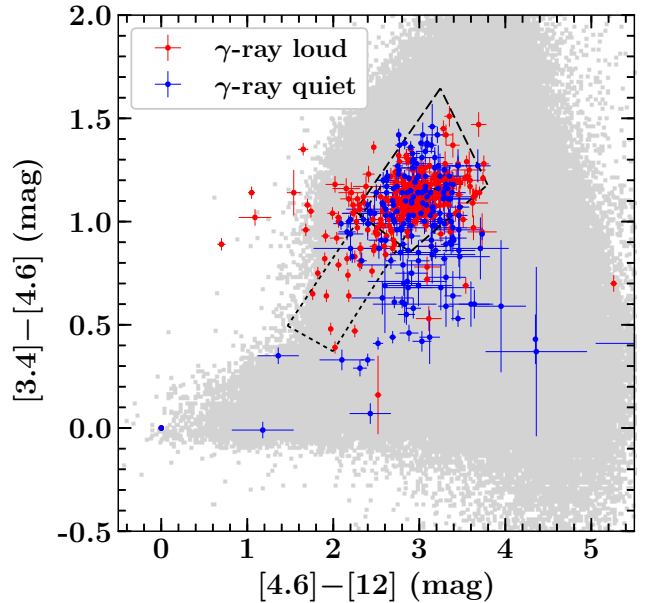


Figure 3. The WISE $[3.4]-[4.6]-[12]$ μm color-color diagram for CGRaBS quasars (red and blue for γ -ray loud and γ -ray quiet objects, respectively) and MQC sources (gray). The black dashed and dotted lines correspond to the WISE Gamma-ray strips for FSRQs and BL Lac objects, respectively (Massaro et al. 2012).

Recently, it has been noticed that *Fermi*-LAT detected blazars occupy a distinct region in the *Wide-field Infrared Survey Explorer* (WISE; Wright et al. 2010) mid-IR color-color diagram, named the *WISE Gamma-ray Strip* (WGS; Massaro et al. 2011). In Figure 3, we show the WISE 3.4–4.6 versus 4.6–12 μm color-color plot for CGRaBS objects and

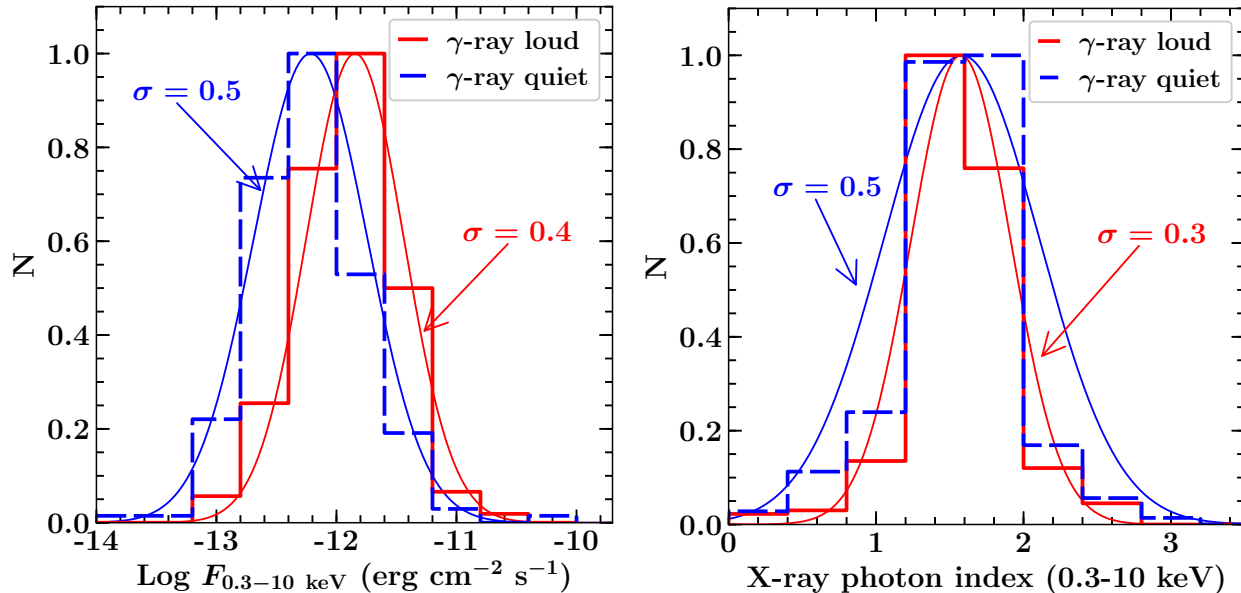


Figure 4. The distribution of the observed 0.3–10 keV X-ray flux (left) and photon index (right) for the γ -ray loud and γ -ray quiet blazars. We show the results only for those sources whose X-ray spectra are fitted with an absorbed power-law model, for an equal comparison. See the text for details.

also include MQC sources for a comparison¹⁰. A majority of the γ -ray loud blazars are found to occupy a narrow region in this diagram (see red points and WGS for FSRQs and BL Lac objects), confirming earlier results. Interestingly, γ -ray quiet blazars are also found to be centered in the same region of the diagram, however with a larger scatter. This can be understood in terms of the origin of the IR emission. As also noticed in D’Abrusco et al. (2012), the observed correlation between 3.4–4.6 μm and 4.6–12 μm colors is tighter for the objects in which both IR and γ -rays originate from the same electron population via synchrotron and SSC/EC mechanisms. On the other hand, the IR emission in FSRQs could be dominated by thermal radiation from the torus and hence may not correlate with the γ -ray emission. Indeed, out of 191 γ -ray quiet blazars 185 are FSRQs, indicating the thermal origin of the IR emission as a possible explanation for the observed scatter.

4.4. X-ray emission

There are *Swift*-XRT observations for a major fraction ($> 90\%$) of CGRaBS quasars. For bright sources (e.g., J1256–0547 or 3C 279), we also find *XMM-Newton* and/or *Chandra* data, though we prefer to use *Swift*-XRT as it allows us to use the simultaneous optical-UV observations from the UVOT. In Table 2 and 3, we present the results of the *Swift*-XRT data analysis for the γ -ray loud and the γ -ray quiet blazars, respectively. Furthermore, for 18 objects (2 γ -ray loud and 16 γ -ray quiet), we could find only *Chandra* or *XMM-Newton* observations, which we use to extract the spec-

tral information in the X-ray band. We report the associated fitting parameters in Table 4.

We compare the X-ray properties of the γ -ray loud and the γ -ray quiet blazars in Figure 4. This is done for the absorbed power-law modeled objects, which constitute a major fraction ($> 93\%$) of the sample, and including all soft X-ray instruments, i.e., *Swift*-XRT, *Chandra*-ACIS, and *XMM-Newton* EPIC-PN. For an equal comparison, we extrapolate *Chandra* analysis results to 10 keV. In the 0.3–10 keV energy range, the γ -ray loud sources ($\langle F_{0.3-10 \text{ keV}} \rangle = 1.4 \times 10^{-12} \text{ erg cm}^{-2} \text{ s}^{-1}$) are brighter than the γ -ray quiet objects ($\langle F_{0.3-10 \text{ keV}} \rangle = 6 \times 10^{-13} \text{ erg cm}^{-2} \text{ s}^{-1}$); however, the spectral slopes ($\langle \Gamma_{0.3-10 \text{ keV}} \rangle = 1.58$ for both) of the distributions are similar (Figure 4), with a slightly larger scatter for γ -ray quiet blazars.

5. MODELING THE BROADBAND EMISSION

The MW SEDs of blazars are often modeled with a one-zone synchrotron-IC model (e.g., Dermer et al. 2009; Ghisellini & Tavecchio 2009; Sikora et al. 2009). We adopt the leptonic emission model of Ghisellini & Tavecchio (2009) to interpret the broadband SEDs of CGRaBS blazars and briefly describe it here. The emission region is considered to have a spherical shape, located at a distance R_{diss} from the central black hole of mass M_{BH} . It moves along the jet axis with a bulk Lorentz factor Γ . Under the assumption of a conical jet with semi-opening angle $\psi = 0.1$ radian, the size of the emission region is constrained from R_{diss} . We assume the initial acceleration phase of the jet by considering $\Gamma \sim \sqrt{R_{\text{diss}}/3R_{\text{Sch}}}$ up to a final value and constant after that (Vlahakis & Königl 2004; Komissarov et al. 2007; Ghisellini & Tavecchio 2009), where R_{Sch} is the Schwarzschild radius.

¹⁰ We determine the *WISE* counterparts within $6''$ of the radio position.

The emission region is assumed to be filled with an electron population that follows a smooth broken power-law energy distribution of the following type

$$S(\gamma) = S_0 \frac{(\gamma_b)^{-p}}{(\gamma/\gamma_b)^p + (\gamma/\gamma_b)^q}. \quad (1)$$

where S_0 is the normalization constant, γ_b represents the peak of the distribution, i.e., the break Lorentz factor, and p and q are the power-law slopes before and after γ_b . The relativistic electrons emit synchrotron and IC radiation in the presence of a uniform but tangled magnetic field. We consider various sources of low energy seed photons that originate both internally and externally to the jet. This includes IC scattering off the synchrotron photons (SSC) and photons radiated from the accretion disk (EC-disk), the BLR (EC-BLR), and the torus (EC-torus). The accretion disk is assumed as a geometrically thin and optically thick disk (Shakura & Sunyaev 1973). Its emission profile has a multi-temperature blackbody shape of the following type (Frank et al. 2002)

$$F_\nu = \nu^3 \frac{4\pi h \cos \theta_\nu}{c^2 D_l^2} \int_{R_{\text{in}}}^{R_{\text{out}}} \frac{R dR}{e^{h\nu/kT(R)} - 1} \quad (2)$$

where h is the Planck constant, θ_ν is the angle between the jet axis and the line of sight, D_l is the luminosity distance, k is the Boltzmann constant, c is the speed of light, and R_{in} and R_{out} are the inner and outer disk radii, assumed as $3R_{\text{Sch}}$ and $500R_{\text{Sch}}$, respectively. The radial dependence of the temperature is given as follows

$$T(R) = \frac{3R_{\text{Sch}} L_{\text{disk}}}{16\pi\eta_{\text{acc}}\sigma_{\text{SB}}R^3} \left[1 - \left(\frac{3R_{\text{Sch}}}{R} \right)^{1/2} \right]^{1/4}, \quad (3)$$

where σ_{SB} is the Stefan-Boltzmann constant and η_{acc} is the accretion efficiency, adopted here as 10%.

We assume that certain fractions of the L_{disk} are reprocessed by the BLR ($f_{\text{BLR}} = 0.1$) and the torus ($f_{\text{torus}} = 0.5$, Ghisellini & Tavecchio 2009). The radiation from the BLR and the torus are adopted to follow a simple blackbody emission profile peaking at the Hydrogen Lyman- α line frequency and at the characteristic temperature (T_{torus}) of the torus, respectively. Both the BLR and the torus are assumed as spherical shells located at distances $R_{\text{BLR}} = 10^{17} L_{\text{d},45}^{1/2}$ cm and $R_{\text{torus}} = 2.5 \times 10^{18} L_{\text{d},45}^{1/2}$ cm, respectively, from the central black hole, where $L_{\text{d},45}$ is the accretion disk luminosity in units of 10^{45} erg s $^{-1}$. We also consider the presence of the X-ray corona lying close to the accretion disk. It reprocesses 30% of the disk radiation. Its spectral shape is considered as $L_{\text{cor}}(\nu) \propto \nu^{-1} \exp(-h\nu/150 \text{ keV})$. We calculate the radiative energy densities of these components in the comoving frame following the prescriptions of Ghisellini & Tavecchio (2009) and use them to derive the EC fluxes.

Jet powers: We estimate the jet power carried by electrons (P_{ele}), Poynting flux (P_{mag}), radiation (P_{rad}), and protons (P_{kin}) as follows (Celotti & Ghisellini 2008)

$$P_k = 2\pi R_{\text{size}}^2 \Gamma^2 \beta_c U'_k, \quad (4)$$

where the factor of 2 accounts for two-sided jets and R_{size} is the size of the emission region. U'_k are the comoving frame energy density of the magnetic field ($k = \text{mag}$), relativistic electrons ($k = \text{ele}$), and cold protons ($k = \text{kin}$) and can be estimated using the following equations

$$U'_{\text{mag}} = B^2/8\pi, \quad (5)$$

$$U'_{\text{ele}} = m_e c^2 \int S(\gamma) \gamma d\gamma, \quad (6)$$

$$U'_{\text{kin}} = m_p c^2 \int S(\gamma) d\gamma, \quad (7)$$

where B is the magnetic field and m_e , m_p are the electron and proton masses, respectively. The radiative power is derived as follows (Ghisellini et al. 2014)

$$P_{\text{rad, EC}} = 2 \frac{4\Gamma^2}{3\delta^4} L_{\text{bol}} \quad (8)$$

$$P_{\text{rad, syn/SSC}} = 2 \frac{16\Gamma^4}{5\delta^6} L_{\text{bol}} \quad (9)$$

where L_{bol} is the bolometric jet luminosity in the observed frame and the factor of 2 accounts for the two-sided jet. To calculate the kinetic power of the jet, we assume an equal number density of electrons and cold protons (e.g., Celotti & Ghisellini 2008).

Black hole mass and the disk luminosity: Two crucial parameters in the blazar SED modeling, particularly in FSRQs, are M_{BH} and L_{disk} . In general, these can be constrained either from single-epoch optical spectroscopy (assuming a virialized BLR, e.g., Shaw et al. 2012) or from fitting the big blue bump at optical-UV energies by a standard Shakura & Sunyaev (1973) disk model (Calderone et al. 2013; Castignani et al. 2013). There are uncertainties associated with both approaches, e.g., the typical errors in the virial spectroscopic black hole mass calculation is ~ 0.4 dex (Vestergaard & Peterson 2006; Shen et al. 2011) and the disk fitting method does not take into account the jet emission. However, when there is a sufficient coverage at optical-UV energies and the big blue bump is visible, the uncertainty in the disk fitting method is quite small (a factor of ~ 2 , Calderone et al. 2013). Both approaches have been thoroughly discussed in Ghisellini & Tavecchio (2015) and we refer an interested reader to this article for details.

We adopt the following steps to determine M_{BH} and L_{disk} for CGRaBS blazars.

1. Whenever we find a big blue bump at IR-UV energies, we reproduce it with a standard accretion disk model and derive both M_{BH} and L_{disk} . We are able to apply this method to 178 γ -ray loud and 176 γ -ray quiet blazars. They are flagged with the keyword ‘D’ in Table 5 and 6.
2. If the bump is not observed or if there are insufficient data points at optical-UV energies, we search in the literature for availability of the optical spectrum (Shen et al. 2011; Shaw et al. 2012; Torrealba et al. 2012). Using the broad emission line ($\text{H}\beta$, Mg II , and C IV) information and the empirical relations of Shen et al. (2011), we determine the mass of the black hole. From the line luminosities, we compute the BLR luminosity following the scaling relations of Francis et al. (1991) and Celotti et al. (1997). Under the assumption that the BLR reprocesses 10% of L_{disk} , we derive the luminosity of the accretion disk. When parameters for more than one line are known, we take the geometric mean of the derived quantities. For 50 γ -ray loud and 5 γ -ray quiet sources, we determine their M_{BH} and L_{disk} via optical spectroscopic measurements. In Table 5 and 6, they are flagged with the keyword ‘O’.
3. When the bump is not visible at optical-UV wavelengths and the optical spectral information is also not available, we adopt an empirical relation between the γ -ray luminosity and the BLR luminosity, as suggested by Sbarrato et al. (2012). It is found that the γ -ray luminosity is a good tracer of the BLR luminosity and the following empirical relation holds (albeit with a large scatter, Sbarrato et al. 2012)

$$L_{\text{BLR}} \sim 4L_{\gamma}^{0.93}. \quad (10)$$

where, L_{BLR} is the BLR luminosity. We then derive L_{disk} from the knowledge of the BLR luminosity. In such sources, we assume a typical M_{BH} of $5 \times 10^8 M_{\odot}$. We compute L_{disk} in 83 γ -ray loud blazars using the empirical method. These objects are flagged with ‘E’ in Table 5.

4. For γ -ray quiet blazars, the previous method could not be used due to lack of γ -ray information. In such sources, we assume an appropriate value of L_{disk} while keeping in mind not to overproduce the observations (i.e., about a factor $\sim 10 - 20$ below the optical-UV data points, e.g., Ghisellini et al. 2010) and also to maintain sub-Eddington L_{disk} and adopt $M_{\text{BH}} = 5 \times 10^8 M_{\odot}$. In 10 γ -ray quiet blazars (i.e., $< 2\%$ of the sample size), this approach is adopted to get an estimation of L_{disk} . These objects can be identified with the flag ‘A’ in Table 6.

SED modeling guidelines: Our SED modeling code does not perform a statistical fitting. We merely reproduce the observations following a ‘fit-by-eye’ approach. Once we have information about the L_{disk} and M_{BH} , as described above, there are eight free parameters in the modeling: p , q , B , R_{diss} , Γ , S_0 , γ_b , and γ_{max} . The size of the emission region is constrained from R_{diss} . Along with this, the following parameters are kept fixed: ψ , θ_v , γ_{min} , T_{torus} , and $f_{\text{BLR/torus/cor}}$ (with rare exceptions). Though our modeling program does not compute uncertainties in the physical parameters, depending on the quality of the MW data, the SED parameters can be fairly well constrained from the observations (e.g., Tavecchio et al. 1998). Below, we briefly elaborate our adopted choices to constrain the free parameters from the observations.

The leptonic model used here fails to reproduce the low frequency (sub-mm to radio) data due to self-absorption of the synchrotron emission. In the low synchrotron peaked objects, however, radio observations provide a clue about the typical flux level of the synchrotron radiation. For many sources, the synchrotron peak lies in the self-absorbed regime. In these objects, the synchrotron peak is the self-absorption frequency. Moreover, the measurement of L_{disk} , either from the disk modeling or from the spectroscopic line measurements, regulates the size of the BLR and the torus, and hence the corresponding radiative energy densities of these components within R_{BLR} and R_{torus} , respectively.

In powerful γ -ray loud blazars, the shape of the γ -ray spectrum directly constrains the high-energy slope of the underlying broken power-law electron energy distribution (q). This slope in turn controls the slope of the high-energy tail of the synchrotron component. The lack of γ -ray information for the γ -ray quiet blazars hampers the determination of q . Since a majority of these sources have disk-dominated optical-UV SEDs, it is also not possible to constrain q from the synchrotron process. However, the *Fermi*-LAT sensitivity limits (shown with black stars in Figure 5) provide us a hint that q has to be steep to avoid the *Fermi*-LAT detection threshold. In FSRQs, the low-energy slope p can be constrained from the X-ray observations. In high synchrotron peaked (HSP) blazars, though, the X-ray spectrum exhibits a steep falling shape, originating from the high-energy tail of the synchrotron component. In such objects, the γ -ray spectrum has a rising shape ($\Gamma_{\gamma} < 2$), and that slope can be used to get an estimation of p .

A rising X-ray spectrum (photon index at 0.3–10 keV $\lesssim 1.5 - 1.6$) in FSRQs hints at a prevailing EC mechanism instead of the SSC process. This is because, in these two processes, not only are the seed photons for IC scattering different but also the participating electrons are of very different energies. In the EC-dominated scenario, the X-ray spectrum originates from the low-energy electron population, whereas relatively high-energy electrons lying close to the peak of the distribution contribute to the observed soft X-ray spectrum

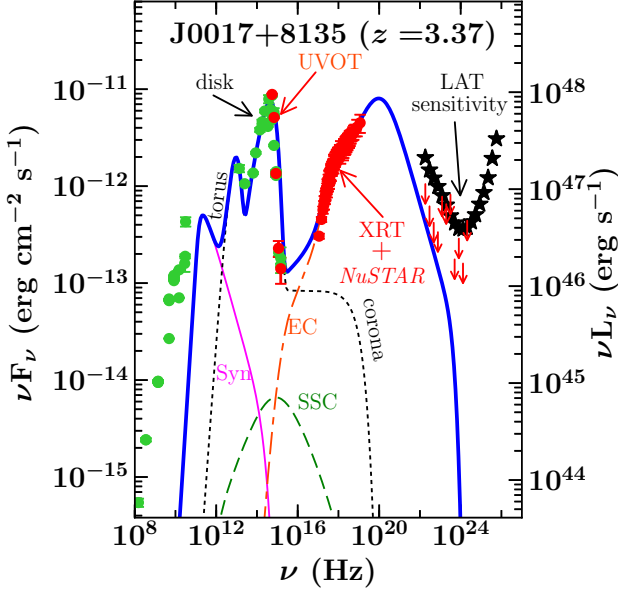


Figure 5. The modeled SED of a γ -ray quiet blazar. Red filled circles represent the data analyzed by us, while the lime-green filled circles are archival observations. The black dotted line corresponds to the thermal emission from the torus, the accretion disk, and the X-ray corona. The pink thin solid line denotes the synchrotron emission. The green long-dashed and orange dash-dash-dot lines represent the SSC and EC processes, respectively. The blue thick solid line is the sum of all of the radiative components. Black stars represent the 3σ *Fermi*-LAT sensitivity for the duration covered in this work and toward the direction of the source. Red downward arrows correspond to the 2σ upper limits. Both sets of information are extracted assuming a photon index of 2.4. The *NuSTAR* data in this source are taken from [Paliya et al. \(2016\)](#). [The modeled SED plots for all other γ -ray quiet blazars are shown in Figs. xxx–xxx in the electronic version.]

via the SSC mechanism (see, a detailed discussion in [Ajello et al. 2016](#)). In other words, a flat X-ray spectrum demands the (softer) SSC component to lie below the observations. This regulates the size of the emission region and the magnetic field. An increase in the magnetic field decreases both the SSC and the EC fluxes for a given flux level of the synchrotron emission. This is due to the fact that with increasing magnetic field, fewer electrons are required to produce the same synchrotron flux. Furthermore, we can also fine tune the bulk Lorentz factor Γ from the X-ray and γ -ray SEDs. For larger Γ , or the Doppler factor δ , fewer electrons are required to make the same flux level of the synchrotron radiation, thus decreasing the synchrotron photon energy density and therefore lowering the SSC flux. However, since the external photon energy densities becomes larger, an increase in δ leads to the enhancement of the EC flux ([Dermer et al. 2009](#); [Ghisellini & Tavecchio 2009](#)).

The Compton dominance (CD), which is the ratio of the high-to-low energy SED peak luminosities, provides us information about the relative prevalence of the external radiation energy densities compared to the magnetic energy density. Since in our model both energy densities are a func-

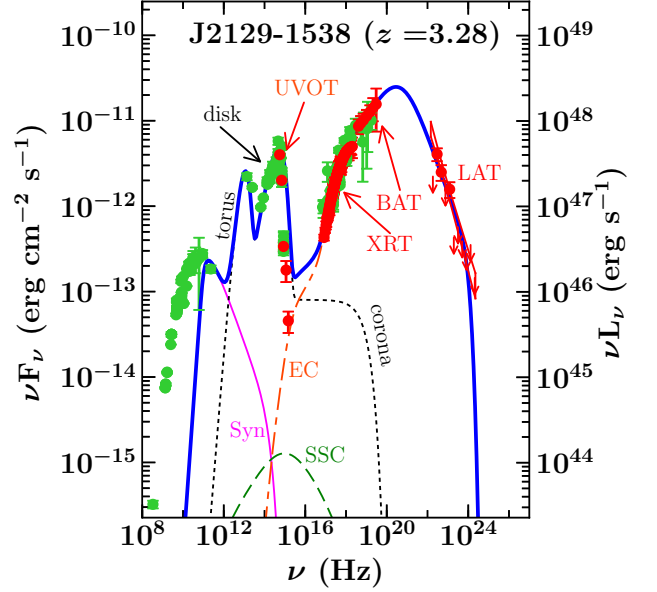


Figure 6. The modeled SED of a γ -ray loud blazar. Other information are same as in Figure 5. [The modeled SED plots for all of the other γ -ray loud blazars are shown in Figs. xxx–xxx in the electronic version.]

tion of R_{diss} (see, [Ghisellini & Tavecchio 2009](#); [Sikora et al. 2009](#)), we can derive the location of the emission region from the observed CD. A large CD (> 1) indicates the dominance of the external photon field, originating from the BLR/torus, and thus suggests the emission region to lie inside the BLR or outside it but still inside the torus. Another constraint comes from the observation of the fast flux variability from many blazars, indicating a compact emission region, which in turn demands the emission region to lie closer to the central black hole (see also, e.g., [Narayan & Piran 2012](#); [Marscher 2014](#), for alternative arguments). On the other hand, comparatively, the EC-torus-dominated SED has a lower CD than the EC-BLR-dominant SED. The high-energy peak located at lower frequencies (\sim MeV energies) also indicates the emission region to be located outside the BLR but inside the torus since a low IC peak probably hints at a smaller characteristic frequency of the seed photons participating in the EC process. A precise determination of CD in γ -ray quiet blazars is rather difficult due to lack of a γ -ray spectrum. However, along with the shape and the flux level of the soft X-ray spectrum, the *Fermi*-LAT sensitivity limit constrains it reasonably well. Whenever the hard X-ray observations are available (see, e.g., Figure 5), CD is even further constrained.

6. PHYSICAL CHARACTERISTICS

The broadband emissions of both γ -ray quiet and γ -ray loud blazars are reproduced using the simple one-zone leptonic emission model described in Section 5. In Figure 5 and 6, we show the modeled SEDs of these two populations, respectively. The parameters associated with the SED modeling are given in Table 5 and 6. We provide the de-

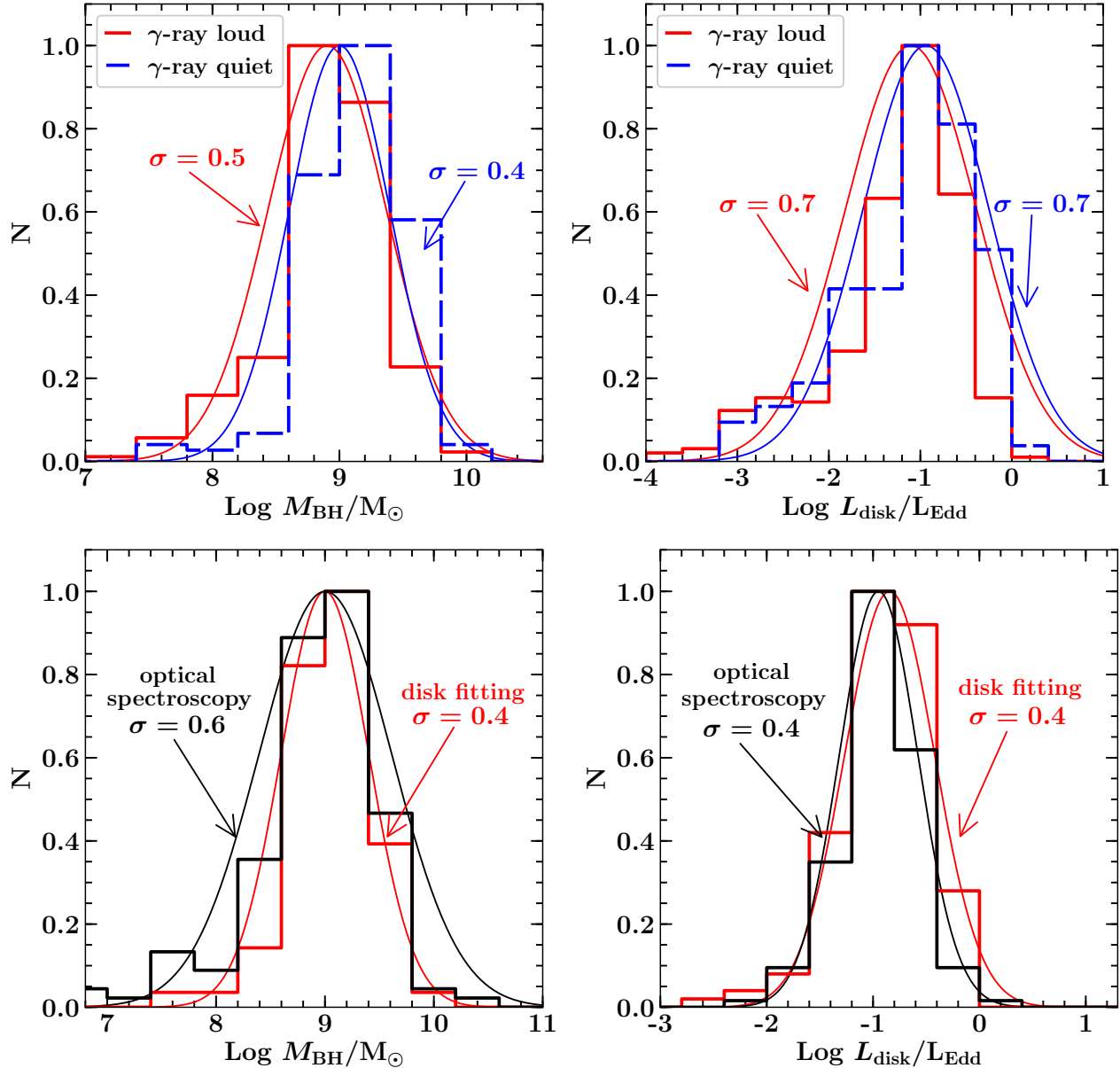


Figure 7. Top: Distributions of M_{BH} and L_{disk} (in Eddington units) for the γ -ray loud (red solid) and the γ -ray quiet (blue dashed) blazars. For an equal comparison the distributions are normalized with the peak set equal to one and we have excluded those sources whose M_{BH} is assumed as $5 \times 10^8 M_{\odot}$. Bottom: Comparison of M_{BH} and L_{disk} (in Eddington units) distributions shown only for those sources that have M_{BH} and L_{disk} computed from the optical spectroscopic (black solid) and disk fitting (red solid) methods. The distributions are fitted with lognormal functions, whose dispersions are indicated.

rived jet powers in Table 7 and 8. The SEDs of 13 γ -ray loud blazars (see Table 9) are well reproduced using synchrotron and SSC emission mechanisms, i.e., without invoking the EC process. All of them are HSP BL Lac objects with synchrotron-dominated SEDs, and they are characterized by featureless optical spectra (e.g., Falomo & Treves 1990; Marcha et al. 1996). Since these objects are modeled without needing the information about L_{disk} and M_{BH} , we do not consider them when we discuss the physical properties of the γ -ray loud blazars associated with L_{disk} and M_{BH} .

6.1. Black Hole Mass and the Accretion Disk Luminosity

In the top panel of Figure 7, we compare M_{BH} and L_{disk} for the γ -ray loud (red) and the γ -ray quiet (blue) blazars. For M_{BH} distributions, we have considered only those objects whose black hole masses are measured either from the optical spectrum or from the disk fitting method, as explained in the previous section. The fitted distribution peaks at $\langle M_{\text{BH}} \rangle \approx 1 \times 10^9 M_{\odot}$ and $8 \times 10^8 M_{\odot}$, for the γ -ray quiet and the γ -ray loud objects, respectively. The fact that the γ -ray quiet blazars host slightly more massive ($\sim 2.5\sigma$ significance) black holes compared to γ -ray loud sources

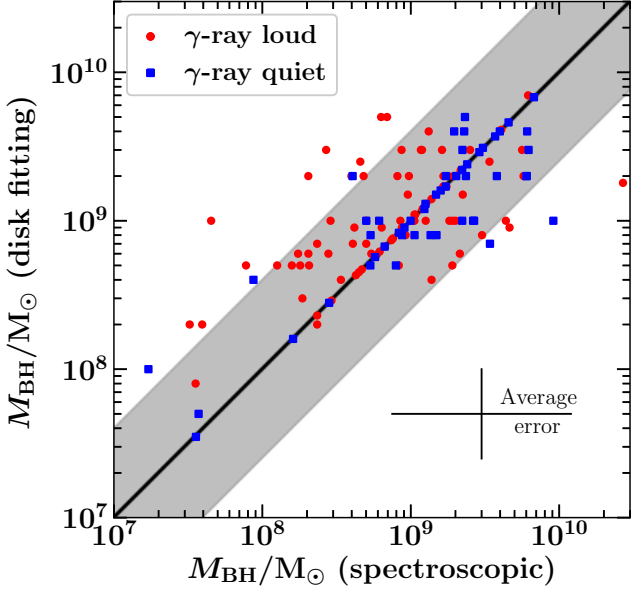


Figure 8. The M_{BH} computed from the optical spectroscopic line information versus that estimated using the disk fitting method. The black solid line is the equality line and the gray shaded region corresponds to a factor of 4 uncertainty in the M_{BH} derived from the optical spectroscopic method (e.g., Vestergaard & Peterson 2006).

can be explained by noting that they are located at larger redshifts (Figure 1), possibly a selection effect of detecting only the heaviest black holes at high redshifts. On the other hand, the accretion disk luminosities in the γ -ray loud and the γ -ray quiet blazars show a similar distribution and peak around 10% of the Eddington luminosity (L_{Edd}). This implies that, in absolute units (i.e., in erg s^{-1}), γ -ray quiet objects host more luminous accretion disks compared to γ -ray loud blazars.

In our sample, there are a total of 138 blazars (86 γ -ray loud and 52 γ -ray quiet) that have M_{BH} and L_{disk} measurements from both the disk fitting and optical spectroscopy methods. Therefore, it is interesting to check the consistency of the results derived from these two different approaches. In the bottom panel of Figure 7, we plot M_{BH} and $L_{\text{disk}}/L_{\text{Edd}}$ distributions estimated from the optical spectroscopic (black) and the disk modeling (red) techniques. The M_{BH} computed from the disk fitting matches well with the virial measurements ($\langle M_{\text{BH}} \rangle = 1 \times 10^9 M_{\odot}$ for both). Fitting the distribution with a log normal function returns a dispersion of 0.4 dex for the disk fitting method and 0.6 dex for the virial masses. Similarly, the distributions of the accretion disk luminosities derived from the disk modeling and the optical emission line approaches show a good agreement. We also show the M_{BH} estimated from the disk fitting method as a function of the M_{BH} derived from the virial approach, for both γ -ray loud and γ -ray quiet blazar populations, in Figure 8. Though there is a large dispersion, overall both results match reasonably. These observations support the argument that the disk modeling could be a robust tool to calculate M_{BH} and L_{disk}

in powerful FSRQs.

6.2. The Particle Distribution

The average properties of the electron energy distribution (EED) can be seen in the top left and middle panels of Figure 9. For both γ -ray loud and γ -ray quiet blazars, the low- and high-energy spectral indices of the EED ($\langle p \rangle = 1.8, 1.7$ and $\langle q \rangle = 3.8, 4.3$, respectively) have a narrow distribution. In powerful FSRQs, the synchrotron peak is typically located at radio to sub-mm frequencies and due to synchrotron self-absorption, it is impossible to characterize the spectral shape of the underlying EED from the synchrotron emission alone. In such blazars, the EED can be constrained using X-ray and γ -ray data, which (in the EC scenario) constrain the spectral shapes of the low-energy and high-energy electron population, respectively. The availability of the *Swift*-BAT or the *NuSTAR* data for a few sources also helps in putting further constraints on the low-energy index p . Note that p regulates the total number of radiating electrons that are present in the emission region, and therefore the total number of protons, which controls the kinetic power of the jet. On the other hand, the distribution of the high energy index q shows a clear bimodality, with the high-energy electron population of the γ -ray loud blazars exhibiting a relatively hard spectrum compared to the γ -ray quiet objects. This can be understood in terms of the non-detection of the γ -ray quiet sources in the γ -ray band. In such sources, a steep falling EC spectrum is necessary to avoid the detection limit of the *Fermi*-LAT (see, e.g., Figure 5). The shape of the optical-UV spectrum can also provide a good constraint to q if it is synchrotron-dominated. However, out of 191 γ -ray quiet blazars we find an accretion-disk-dominated optical-UV SED in 176 sources, implying q is rather unconstrained from the synchrotron emission.

We show the distribution of the break Lorentz factor (γ_{b}) and the maximum Lorentz factor (γ_{max}) of the EED in the top right and middle left panels of Figure 9. In both plots, the distribution of the γ -ray quiet blazars is relatively low peaked ($\langle \gamma_{\text{b}} \rangle \sim 56$ and $\langle \gamma_{\text{max}} \rangle \sim 2000$) and has narrower dispersion, when fitted with a log normal function. The wider distributions for the γ -ray loud blazars are probably due to the presence of a few HSP BL Lac objects such as J1653+3945 (or Mrk 501). These sources have their synchrotron peak located at very high frequencies ($> 10^{16}$ Hz), thus implying the peak of the underlying EED, i.e., γ_{b} , to have a large value. Furthermore, γ_{max} is rather insensitive to the modeling for the steeply falling γ -ray spectrum FSRQs. However, a hard rising γ -ray spectrum in HSP sources indicates a large γ_{max} . This is the reason that the distribution of γ_{max} for the γ -ray loud population extends to very large values and accordingly is centered at a larger γ_{max} of ~ 4000 (Figure 9).

6.3. Magnetic Field and the Location of the Emission Region

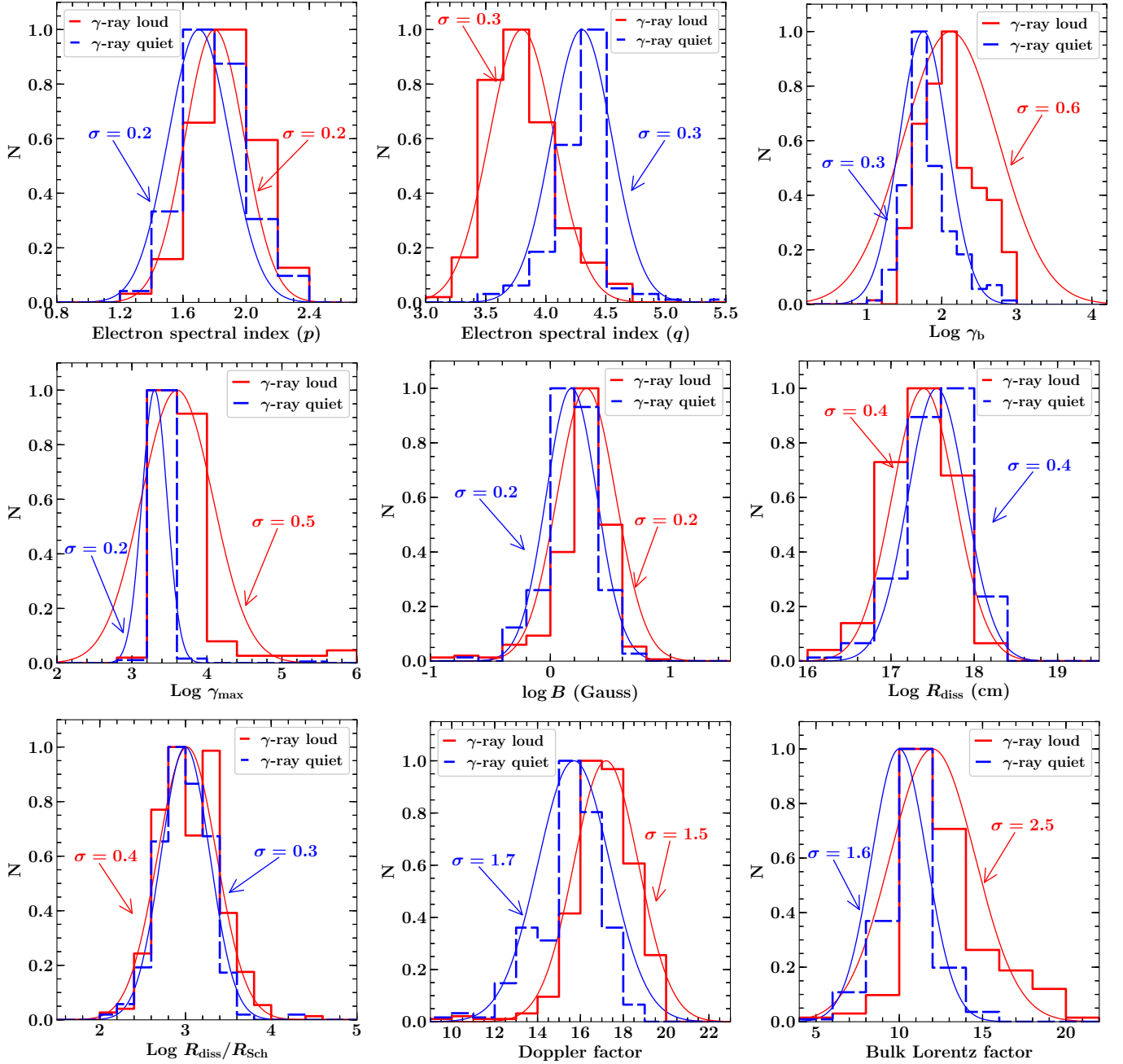


Figure 9. Distributions of the particle spectral indices before (p , top left) and after (q , top middle) the break energy (γ_b , top right), the maximum Lorentz factor (γ_{\max} , central left), the magnetic field (central middle), distance of the emission region from the central black hole in cm (central right) and in R_{Sch} (bottom left), the Doppler factor (bottom middle) and the bulk Lorentz factor (bottom right).

The distribution of the magnetic field for the γ -ray loud blazars peaks around $\langle B \rangle = 2.0$ Gauss, whereas, for γ -ray quiet sources it is centered at a low value of 1.5 Gauss (see middle plot in the middle panel of Figure 9). Fitting them with a log normal function returns a narrow width of 0.2 dex for both distributions.

The logarithmic distribution of the location of the emission region in absolute units (cm) peaks at $\langle R_{\text{diss}} \rangle = 2.5 \times 10^{17}$ cm and 3.5×10^{17} cm for the γ -ray loud and the γ -ray quiet blazars, respectively (middle right panel of Figure 9).

Fitting the distributions with a log normal function gives an equal dispersion of 0.4 dex for both of them. On the other hand, considering the dissipation distance in units of R_{Sch} , we find no difference in the distributions of γ -ray loud and γ -ray quiet sources. On average, the emission region is found to be located inside the BLR for a majority of sources.

6.4. Doppler and the Bulk Lorentz Factors

The distributions of δ and Γ are shown in the bottom middle and right panels of Figure 9. On average, the γ -ray

loud blazars exhibit a larger δ and Γ ($\langle\delta\rangle = 17.2$, $\langle\Gamma\rangle = 12$) compared to the γ -ray quiet blazars ($\langle\delta\rangle = 15.7$, $\langle\Gamma\rangle = 10$). Recently, based on the radio study of 1.5 Jy MOJAVE AGNs, [Lister et al. \(2015\)](#) have reported that the γ -ray detected blazars have significantly larger Doppler boosting factors compared to sources not detected by *Fermi*-LAT (see also, [Savolainen et al. 2010](#), and references therein, for earlier results). The similarity of the results derived from two different approaches, from the SED modeling and the 15 GHz radio measurements, is rather striking. We emphasize here that the lower δ of the γ -ray quiet blazars may not be due to a large θ_v or misalignment of the jet (see also, [Meyer et al. 2011](#)). It is primarily due to small Γ and can be explained as follows. In a majority of the FSRQs studied here, the X-ray to γ -ray SEDs are explained by the EC process (e.g., Figure 5 and 6). The EC mechanism has a stronger dependence on θ_v , and due to anisotropy of the external radiation field in the comoving frame of the emission region, it has an additional boosting ([Dermer 1995](#)). A hard-rising EC emission at X-rays indicates a small θ_v and vice-versa. In other words, the X-ray spectrum in EC-dominated blazars can be used as a tool to determine θ_v (e.g., [Sbarrato et al. 2013](#)). We find the X-ray spectral shapes of both the γ -ray loud and the γ -ray quiet blazars to be similar (Figure 4), thus indicating a similar θ_v , which is further confirmed from the SED modeling (Table 5 and 6).

6.5. Jet powers

Figure 10 represents the distributions of various jet powers. As can be seen, the γ -ray loud and the γ -ray quiet blazars share a similar distribution of the power carried by relativistic electrons, Poynting flux, and cold protons. However, the γ -ray loud sources exhibit a larger P_{rad} compared to the γ -ray quiet objects. This is probably due to γ -ray emitting jets being more radiatively efficient. Also, P_{ele} is substantially less than P_{rad} . This is the direct consequence of the rapid cooling of electrons in a time substantially smaller than the light crossing time of the emission region, so that more power is released in the form of radiation than remains in electrons. The fact that P_{mag} is slightly lower than P_{rad} indicates that the magnetic field alone is not responsible for the observed radiation. This leaves us to consider P_{kin} as a plausible reservoir for P_{rad} . In fact, most of the jet power remains in the form of dynamically dominant protons which produce the large scale radio structures. Only a small fraction ($\sim 1 - 10\%$, see also the top panel of Figure 11) of it gets converted to radiation. We have assumed an equal number density of electrons and cold protons. This assumption is crucial and often leads to the total jet power in powerful FSRQs to exceed L_{Edd} (e.g., [Ghisellini et al. 2014](#)). Considering the presence of the electron-positron pairs would reduce the budget of the jet power (see, e.g., [Madejski et al. 2016](#); [Pjanka et al. 2017](#)); however, their number cannot be large ($\lesssim 10$ -15 pairs per proton, e.g., [Sikora & Madejski 2000](#); [Celotti &](#)

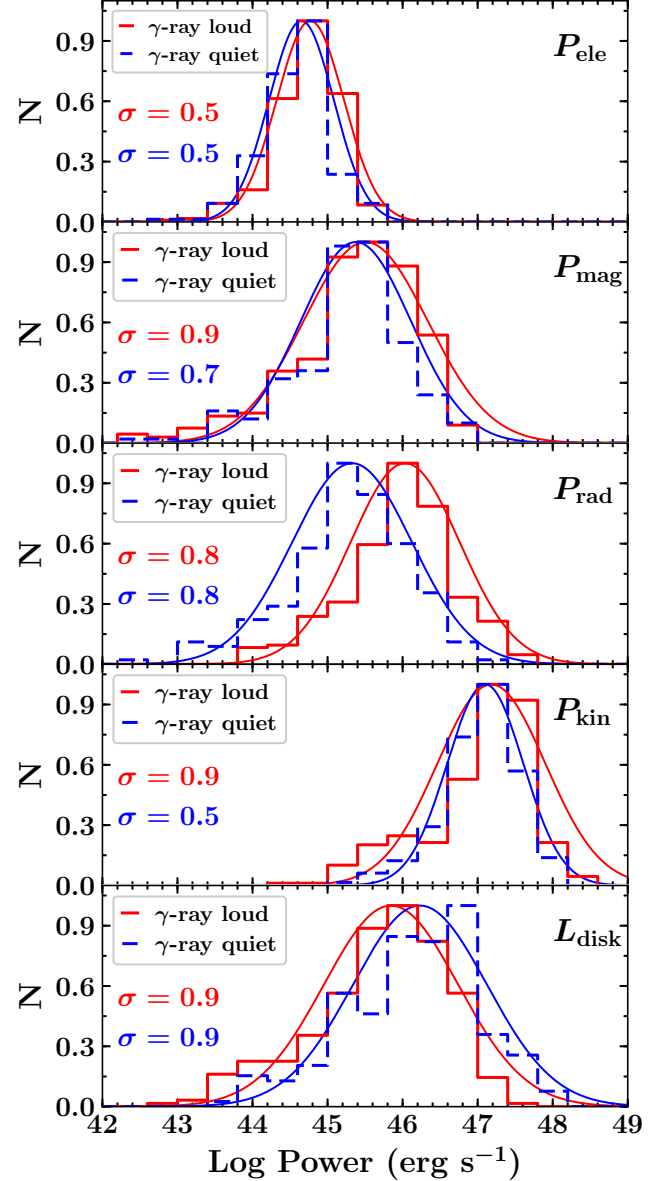


Figure 10. Distributions of various jet powers considering two-sided jets. In the bottom panel, we also show the distribution of L_{disk} for a comparison with the jet power. The histograms are fitted with a log normal function and the corresponding widths are quoted. The average values of the distributions, for the γ -ray loud and the γ -ray quiet blazars, respectively, are as follows: $\langle\log P_{\text{ele}}\rangle = 44.76, 44.65$, $\langle\log P_{\text{mag}}\rangle = 45.48, 45.38$, $\langle\log P_{\text{rad}}\rangle = 45.99, 45.33$, $\langle\log P_{\text{kin}}\rangle = 47.15, 47.10$, and $\langle\log L_{\text{disk}}\rangle = 45.85, 46.23$. All units are in erg s^{-1} .

[Ghisellini 2008](#)) to avoid the Compton rocket effect ([Odell 1981](#)). If present in a substantial fraction, these pairs would produce a large amount of soft X-radiation (so-called the ‘‘Sikora bump’’), which is yet to be observed. Alternatively, instead of a uniform one-zone emission, if one considers the broadband emission to originate from a spine-sheath structured jet, the total power of the jet will come down ([Sikora et al. 2016](#)). Moreover, as can be seen in Figure 10, P_{mag} is tiny compared to P_{kin} and hints at a weak magnetization

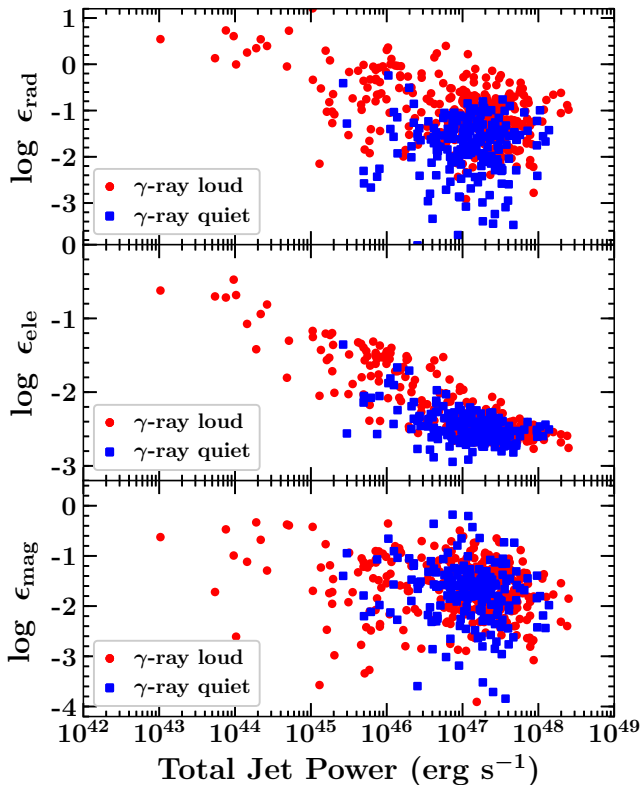


Figure 11. The fraction of the total jet power transformed into radiation (ϵ_{rad} , top), relativistic electrons (ϵ_{ele} , middle), and Poynting flux (ϵ_{mag} , bottom).

of the emission region. These observations, therefore, argue against the Poynting-flux-dominated scenario (e.g., McKinney et al. 2012, but see, Nalewajko et al. 2014; Janiak et al. 2015; Zdziarski et al. 2015).

In Figure 11, we show the fraction of the total jet power ($P_{\text{jet}} = P_{\text{ele}} + P_{\text{mag}} + P_{\text{kin}}$) converted to radiation (ϵ_{rad}), carried by relativistic electrons (ϵ_{ele}), and magnetic field (ϵ_{mag}). It can be seen in the top panel of this plot that there are a few low-power blazars that have $\epsilon_{\text{rad}} \gtrsim 1$. These are primarily BL Lac objects that are known to exhibit $P_{\text{rad}} \sim P_{\text{kin}}$. In these sources, almost all of the available jet power is used to produce the radiation (see, Ghisellini et al. 2010, for a relevant discussion).

7. DISCUSSION

By applying a simple leptonic emission model, we are able to study a few fundamental physical properties of blazars, which are briefly discussed in the following sub-sections. In order to determine the strength of the correlations, we compute the Spearman’s rank-correlation coefficient (ρ_s) and the probability of no correlation, PNC. Since we do not have error estimation for the derived SED parameters, we quantify the strength of the correlation by performing a Monte Carlo simulation following a bootstrapping approach that takes into account the dispersion of the plotted quantities. We create 10^4 data sets, each consisting of N data pairs x_i and y_i (N is

the sample size) and compute ρ_s and PNC for each data set. A pair (x_i, y_i) is randomly chosen from the original data set such that some of the original pairs may appear more than once in a given data set or not at all. Assuming that the returned values follow a Gaussian distribution, we estimate the correlation coefficient and the 1σ uncertainty by deriving the average and the standard deviation of the calculated values. Quoted PNC values are the average of the calculated PNC in each simulation. Note that it can be argued that the observed correlations could be due to intrinsic correlations of the input SED parameters. However, in our work, the chosen modeling parameters are independent and they are constrained only by the observations, thus supporting the connection of the observed correlations with the physical behavior of the sources. In various correlation plots, the reported average errors are 1σ standard deviation of the plotted parameters for the whole population, i.e., including both γ -ray loud and γ -ray quiet blazars, unless specified.

7.1. Accretion-Jet Connection in Blazars

There are evidences for a positive correlation between the jet power and the accretion luminosity in jetted AGNs (e.g., Rawlings & Saunders 1991). More importantly, it has been claimed, both from theoretical and observational arguments, that the former exceeds the latter (Celotti & Ghisellini 2008; Tchekhovskoy et al. 2011; Ghisellini et al. 2014). We test these hypotheses on CGRaBS quasars.

In the top panel of Figure 12, we show the variation of P_{rad} as a function of L_{disk} . The results of the correlation analysis are provided in Table 10. Overall, we find a strong positive correlation ($\rho_s = 0.63 \pm 0.03$, $\text{PNC} < 1 \times 10^{-5}$), which remains valid if we consider the γ -ray loud and the γ -ray quiet blazar populations separately (Table 10). However, since both L_{disk} and P_{rad} depend on redshift, we also perform a partial correlation test by following the prescriptions of Padovani (1992). Even after excluding the common redshift dependence, both L_{disk} and P_{rad} still correlate, although the significance becomes a bit weaker ($\rho_{\text{par}} = 0.19 \pm 0.08$, $\text{PNC} < 1 \times 10^{-5}$). Interestingly, a major fraction of the γ -ray loud blazars lie above the best fit (black dashed line) and except for a few sources, almost all of the γ -ray quiet objects occupy the low P_{rad} regime. This is probably due to the fact that the γ -ray loud blazars are more radiatively efficient than the γ -ray quiet blazars, although they share a similar range of L_{disk} .

We show the variation of the total jet power, P_{jet} , as a function of the total available accretion power ($\dot{M}c^2$) in the bottom panel of Figure 12. Note that for a maximally rotating black hole, the efficiency of accretion is $\eta_{\text{acc}} = 0.3$ (Thorne 1974), and we have $\dot{M}c^2 = L_{\text{disk}}/\eta_{\text{acc}}$. The results of the correlation analysis suggest a strong positive correlation, which remains valid even after removing the common redshift dependence (Table 10). Therefore, we confirm the earlier findings about the accretion-jet connection,

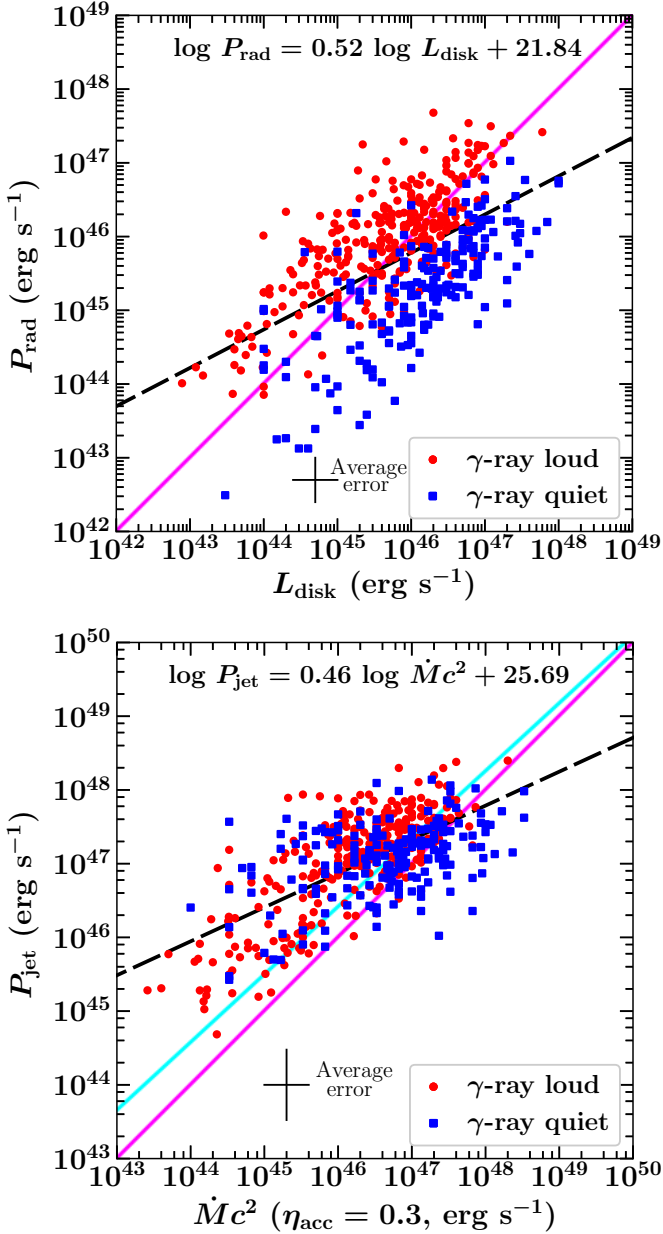


Figure 12. The disk-jet connection in blazars. Top: The plot of P_{rad} versus the L_{disk} for the γ -ray loud (red) and the γ -ray quiet (blue) blazars. Bottom: The jet power versus the total accretion power, assuming an accretion efficiency $\eta_{\text{acc}} = 0.3$. In both plots, the pink solid line represents the one-to-one correlation and the black dashed line denotes the best fit. In the bottom panel, the cyan solid line shows the correlation reported by Ghisellini et al. (2014). The uncertainties in both P_{rad} (corresponding to the uncertainty in Γ^2) and L_{disk} are a factor of 2, the same as that in $\dot{M}c^2$. On the other hand, the average uncertainty in P_{jet} is a factor of 3 (e.g., Ghisellini et al. 2014).

considering both γ -ray loud and γ -ray quiet blazar populations. However, comparing our results with the ones derived by Ghisellini et al. (2014), we notice an interesting observation. In our sample, there are many γ -ray quiet blazars that have larger L_{disk} but host a relatively moderate power jet. As can be seen in Figure 12, almost all γ -ray loud blazars lie

above the one-to-one correlation (pink solid line) but there are many γ -ray quiet blazars that are located below. Accordingly, the slope of the best fitted line in our case is softer. In other words, the fact that the jet power exceeds the accretion power is probably true for the γ -ray loud sources; however, we may see a deviation from this trend when considering a larger γ -ray quiet blazar population.

7.2. Black Hole Mass Dependence

In Figure 13, we show the redshift dependence of M_{BH} derived in this work. Note that we consider only those objects whose M_{BH} are computed either from the disk fitting or the optical spectroscopic methods. For a comparison, we also show M_{BH} values for SDSS quasars as reported in Kozłowski (2017). The results of the correlation analysis suggest a positive correlation between M_{BH} and redshift (Table 10), which is probably a selection effect. Furthermore, we plot L_{disk} , P_{jet} , and CD as a function of the derived masses in Figure 13. All three correlate positively with M_{BH} . However, since L_{disk} , P_{jet} and M_{BH} are a function of the redshift, we also perform partial correlation tests to exclude the common redshift dependence. As can be seen in Table 10, even after subtracting the redshift effect, L_{disk} shows a positive correlation with M_{BH} ($\rho_s = 0.39 \pm 0.06$, $\text{PNC} < 1 \times 10^{-5}$), whereas P_{jet} is very weakly correlated ($\rho_s = 0.17 \pm 0.09$, $\text{PNC} < 1 \times 10^{-5}$), considering the entire sample. We also find a positive correlation between CD and M_{BH} . However, since CD, being the ratio of two luminosities, is a redshift-independent quantity whereas M_{BH} is not, we adopt a semi-partial correlation analysis to exclude the redshift dependence of M_{BH} . The results of this exercise lead to the conclusion that CD does not correlate with M_{BH} (see Table 10). Although massive black-hole-hosted blazars are known to be Compton dominated (e.g., Paliya et al. 2016), our correlation analysis indicates that even blazars with low mass black holes can also have a large CD (> 1). The *Fermi*-LAT detected narrow line Seyfert 1 galaxies¹¹ are probably a good example of this (e.g., Paliya et al. 2013).

7.3. Blazar Sequence

There has been a long debate about the validity of the blazar sequence (Fossati et al. 1998), i.e., whether such a sequence has a physical origin (Ghisellini et al. 1998) or is just a selection bias (e.g., Giommi et al. 2012a). In the physical scheme, the rate of accretion onto the central compact object can explain the observed phenomena. A luminous disk implies an efficient accretion process ($L_{\text{disk}}/L_{\text{Edd}} \gtrsim 1 \times 10^{-2}$), which ionizes the BLR clouds resulting in the detection of the broad optical emission lines. Accordingly, the jet electrons interact with the dense photon field of the BLR via EC

¹¹ Narrow line Seyfert 1 galaxies are known to host low-mass black holes (e.g., Yuan et al. 2008).

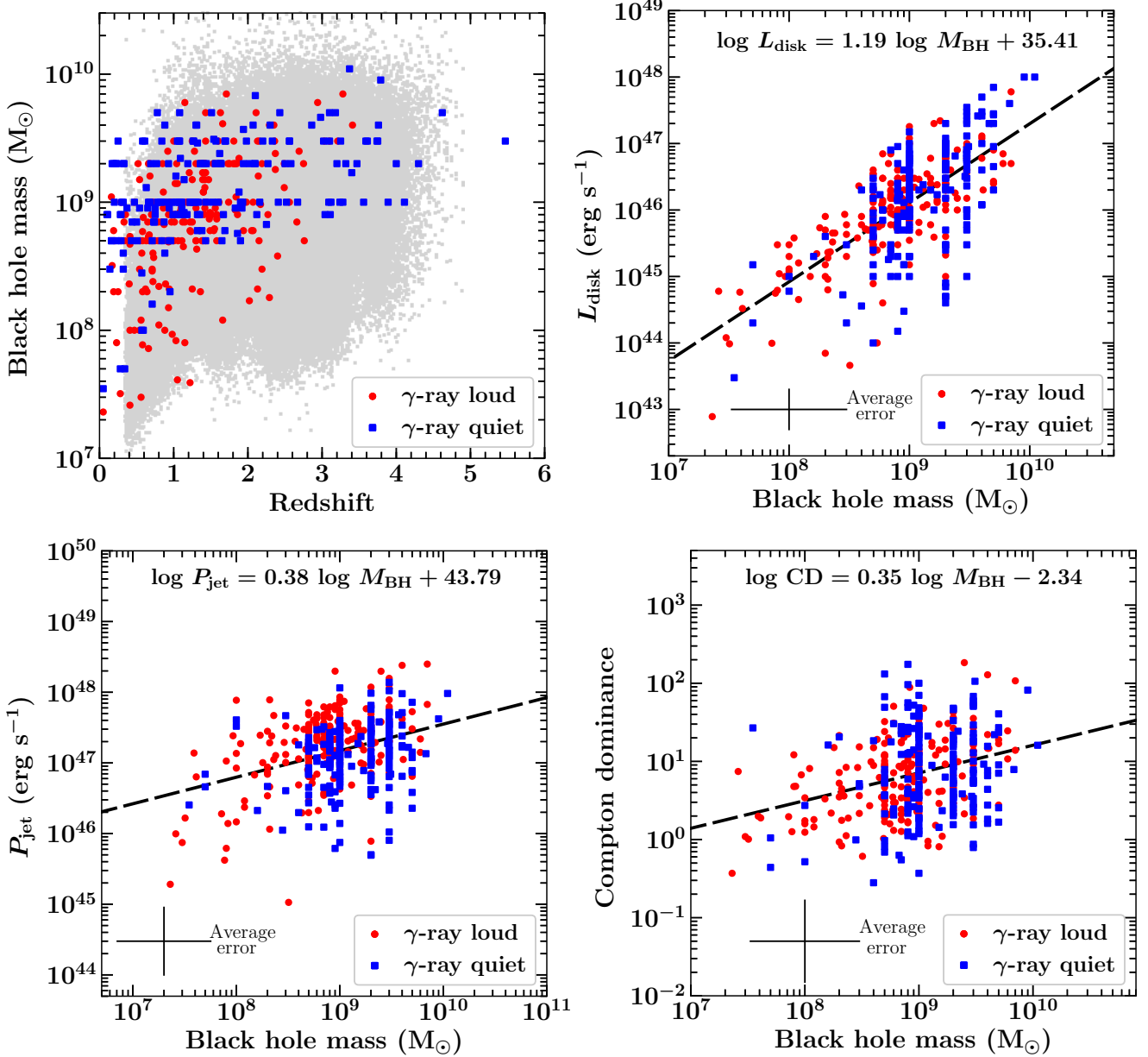


Figure 13. Top left: The redshift dependence of M_{BH} for the γ -ray loud (red) and the γ -ray quiet blazars (blue). The gray dots correspond to SDSS quasars (Kozłowski 2017). The accretion luminosity L_{disk} (top right), the total jet power P_{jet} (bottom left), and the Compton dominance (bottom right) are shown as a function of the derived black hole masses. In all of the plots, the black dashed line is the best fit. The quoted uncertainty in the black hole mass is a factor of 3, which is the average of that typically reported for the disk fitting and virial estimation methods (e.g., Vestergaard & Peterson 2006; Castignani et al. 2013).

mechanism before reaching high energies and produce luminous γ -ray emission, which makes the SEDs more Compton dominated and low-frequency peaked. On the other hand, in the low-accretion regime ($L_{\text{disk}}/L_{\text{Edd}} < 1 \times 10^{-2}$), the external radiation field becomes weaker and the SED is less Compton dominated. We test these hypotheses on our sample of CGRaBS quasars and show the results in Figure 14.

We find a significant anti-correlation between L_{disk} (in Eddington units) and γ_{b} ($\rho_{\text{s}} = -0.30 \pm 0.05$, $\text{PNC} < 1 \times 10^{-5}$). This suggests that an increase in L_{disk} corresponds to a decrease in γ_{b} , i.e., the shift of the SED peaks to lower frequen-

cies. Moreover, we also find that L_{disk} and R_{diss} are strongly anti-correlated ($\rho_{\text{s}} = -0.64 \pm 0.03$, $\text{PNC} < 1 \times 10^{-5}$). Both anti-correlations indicate a physical connection between L_{disk} and the behavior of the SED in blazars. As discussed above, a stronger accretion disk emission implies a luminous BLR whose intense radiation field interacts with jet electrons making them lose energy primarily via EC-BLR process. This also hints that the stronger the disk emission, the closer the location of the dissipation region to the central black hole (with respect to the outside BLR scenario), which is observed.

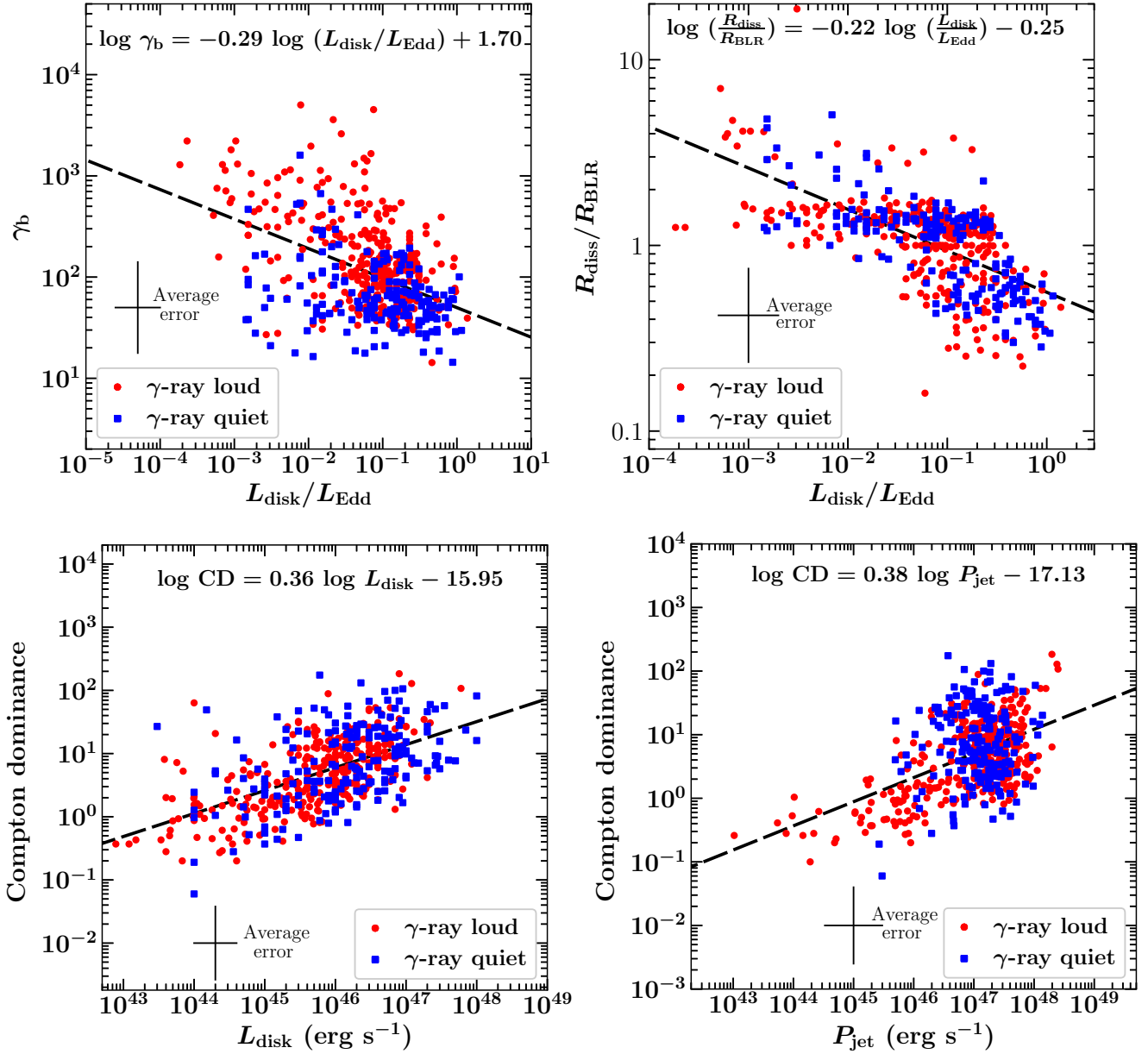


Figure 14. Top: The variations of γ_b (left) and the dissipation distance (right, in units of the BLR radius) as a function of the accretion luminosity (in Eddington units). The pink solid lines represent the inner and outer boundaries of the BLR. The emission region is located inside or close to the outside of the inner boundary of the BLR for objects with a large L_{disk} . Bottom: The Compton dominance as a function of L_{disk} (left) and P_{jet} (right). A significant positive correlation is found. In all plots, the black dashed line represents the best fit.

In the bottom panels of Figure 14, we show the variation of CD with respect to L_{disk} and P_{jet} . In both cases, strong positive correlations are found that remain significant for CD versus L_{disk} and become weaker for CD versus P_{jet} , after excluding the redshift dependence by means of a semi-partial correlation analysis (Table 10). This implies that more Compton-dominated blazars host more powerful disks. Connecting these findings with those discussed above, we can conclude that the accretion disk plays a major role in controlling the observed properties of powerful blazars, and this supports the claim that the blazar sequence has a physical origin (see also, Ghisellini et al. 2017). However, it may be

worth revisiting this hypothesis by including a large sample of BL Lac objects, especially high-redshift ones (see, e.g., Kaur et al. 2017).

7.4. Blazar Evolution Scenario

We show the redshift dependence of L_{disk} , P_{jet} and CD in Figure 15, and the associated correlation parameters are reported in Table 10. The positive correlations observed in L_{disk} and P_{jet} are most likely the Malmquist bias. However, a positive correlation of CD with redshift appears more like an evolutionary effect naturally related to redshift since CD is a redshift-independent quantity. One can argue that such

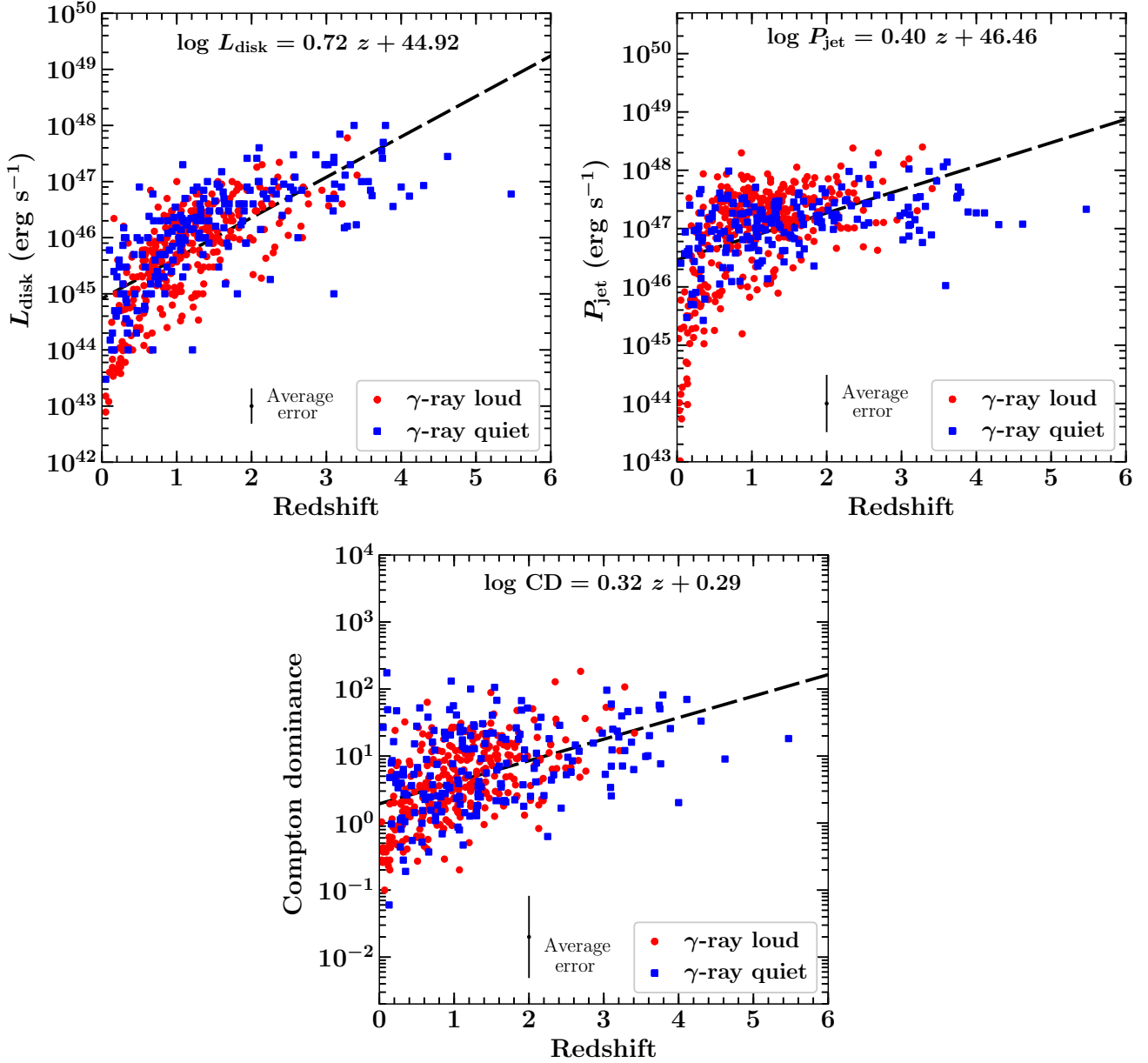


Figure 15. Cosmic evolution of L_{disk} , P_{jet} and CD as observed in γ -ray loud and γ -ray quiet blazars.

a correlation could be spurious since CD exhibits a positive correlation with L_{disk} , which itself strongly depends on redshift. However, as we have shown earlier (see Table 10 and Figure 14), CD and L_{disk} are intrinsically correlated. Our results are in line with the findings of Böttcher & Dermer (2002) and Cavaliere & D’Elia (2002), indicating the evolution of the high power, Compton-dominated sources to the less-luminous, low Compton-dominated ones. We caution, however, that a strong claim cannot be made for the following two reasons. First, there are very few objects in our sample beyond redshift 3, and without γ -ray detection that poses difficulty in accurately measuring their IC peak luminosity and hence CD. Second, only a minor fraction of our sample are BL Lac objects, which are typically low-CD sources

(e.g., Tavecchio et al. 2010), and it is possible that such objects could be located at high redshifts (see, e.g., Kaur et al. 2017). In our future work, we will try to address these shortcomings by considering more BL Lac sources and γ -ray detected high-redshift blazars (Ackermann et al. 2017).

7.5. Gamma-ray Loud versus Gamma-ray Quiet Blazars

Fermi-LAT has detected hundreds of blazars in its first four years of observation (Ackermann et al. 2015), but an even larger number are yet to be detected in γ -rays (Massaro et al. 2015). It was found in several radio studies that the γ -ray quiet blazars have lower Doppler boosting factors. Lister et al. (2015) have reported the synchrotron peaks of the γ -ray quiet sources to be located at relatively lower frequencies

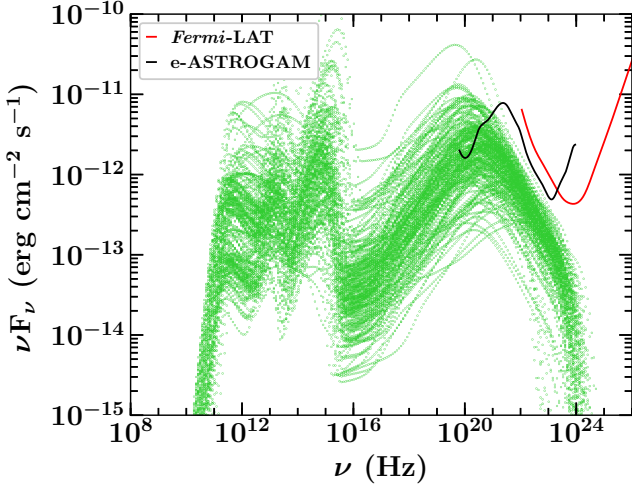


Figure 16. The broadband SEDs of all of the γ -ray quiet blazars studied in this work (lime green). Overplotted are the *Fermi*-LAT sensitivity in 10 years of observation (red) and the 3σ sensitivity plot for 1 year of exposure of the proposed all-sky MeV mission e-ASTROGAM (black).

($< 10^{13.4}$ Hz), implying their high-energy IC peak to lie below the energy range covered by the *Fermi*-LAT. These objects are therefore less likely to be γ -ray detected. According to our analysis, the γ -ray loud and γ -ray quiet blazars share several similar observational features such as occupying the same region in the *WISE* color-color diagram (albeit with a large scatter in the γ -ray quiet objects). The M_{BH} and L_{disk} distributions of the γ -ray loud sources are also similar with those derived from the γ -ray quiet blazars. However, the γ -ray loud blazars are relatively brighter in the radio and X-ray bands, and they exhibit larger Doppler factors compared to their γ -ray quiet counterparts. The γ -ray emission in powerful blazars is produced via the EC process (in the leptonic emission scenario), which is very sensitive to the Doppler boosting because of the anisotropic nature of the external radiation field in the emission region frame (Dermer 1995). Therefore, the difference in the Doppler boosting could account for the γ -ray non-detection. Another crucial parameter that we find significantly different in the γ -ray loud and the γ -ray quiet blazars is the break Lorentz factor, γ_b . In our SED modeling, we have constrained γ_b from the location of the synchrotron peak. Since in one-zone leptonic modeling the same electron population radiates the high energy X-ray to γ -ray emission, γ_b also controls the location of the IC peak according to the following relation (e.g., Sahayanathan & Godambe 2012)

$$\nu_{\text{Syn}} \approx \frac{\delta}{1+z} \gamma_b^2 \nu_L \quad (11)$$

$$\nu_{\text{SSC}} \approx \frac{\delta}{1+z} \gamma_b^4 \nu_L \quad (12)$$

$$\nu_{\text{EC}} \approx \frac{\Gamma \delta}{1+z} \gamma_b^2 \nu_{\text{seed}} \quad (13)$$

where ν_L is the Larmor frequency and ν_{seed} is the characteristic frequency of the BLR/torus photon field. As can be seen in the top right panel of Figure 9, γ -ray quiet blazars have smaller γ_b compared to γ -ray loud sources, thus indicating their IC peak to be located at lower frequencies. In other words, they are more MeV-peaked. A shift of the IC peak to low frequencies makes their falling part of the EC spectrum steeper and thus avoids detection by the *Fermi*-LAT. The fact that the γ -ray quiet blazars are bright in the MeV band makes them suitable targets for observations from the facilities like *NuSTAR* (Harrison et al. 2013). The ideal instrument, however, would be an all-sky survey MeV mission, e.g., e-ASTROGAM (De Angelis et al. 2016) or AMEGO¹². In Figure 16, we plot the modeled SEDs of all of the γ -ray quiet blazars (lime green) and overplot the 3σ flux sensitivity of e-ASTROGAM (black line) for 1 year of observation. For comparison, we also show the flux sensitivity of the *Fermi*-LAT (red line) for its 10 years of operation for high Galactic latitude sources. As can be seen, the chances of *Fermi*-LAT detection for these sources are remote unless they exhibit high-amplitude flaring activity with a shift of the IC peak to higher frequencies (see, e.g., Abeysekara et al. 2015, for the detection of such an event that led to the detection of the FSRQ PKS 1441+25, $z = 0.94$, at TeV energies). On the other hand, according to Figure 16, 121 γ -ray quiet blazars would be detected by e-ASTROGAM (at 500 keV) in one year of observations. Our study of γ -ray quiet blazars, therefore, presents a potential list of blazars to be detected by future MeV missions.

8. SUMMARY

In this work, we have performed a broadband study of a large sample of blazars included in the CGRaBS catalog (Healey et al. 2008). Our main findings are as follows

1. The γ -ray loud and the γ -ray quiet objects do not show a major difference in the *WISE* color-color diagram, and their X-ray spectral shapes are also similar. However, γ -ray loud blazars are brighter in the radio and X-ray bands.
2. A comparison of M_{BH} and L_{disk} derived from the disk fitting and optical spectroscopic approaches leads to similar results, thus suggesting that disk modeling could be used as a robust diagnostic to derive M_{BH} and L_{disk} in powerful blazars.
3. Both γ -ray loud and γ -ray quiet blazars exhibit similar distributions of M_{BH} and L_{disk} with γ -ray quiet sources hosting slightly more massive ($\sim 2.5\sigma$ significance) black holes.

¹² https://pcos.gsfc.nasa.gov/physpag/probe/AMEGO_probe.pdf

4. We find a considerable difference in the Doppler factors of the γ -ray loud and the γ -ray quiet blazars, with γ -ray loud sources more boosted. These results confirm the earlier findings derived from radio observations.
5. The γ -ray loud blazars have a larger jet power in radiation compared to the γ -ray quiet objects. This implies that the jets in the γ -ray loud blazars are more radiatively efficient.
6. We confirm that the accretion process and the jet are positively correlated, an effect that remains significant even after excluding the common redshift dependence. For a majority of the sources the jet power exceeds the accretion luminosity; however, many γ -ray quiet blazars have more powerful disks than their jets. Therefore, it is possible that we may see a deviation from the observed trend ($P_{\text{jet}} > L_{\text{disk}}$) when one considers a larger sample of the γ -ray quiet blazars.
7. Both L_{disk} and P_{jet} show a positive correlation with M_{BH} , which remains strong for L_{disk} and becomes weaker for P_{jet} after excluding the common redshift dependence. On the other hand, the results of the semi-partial correlation analysis has led to the conclusion that CD does not correlate with M_{BH} , implying that even blazars hosting low-mass black holes can be Compton dominated. The γ -ray emitting narrow line Seyfert 1 galaxies are a good example of such objects.
8. According to our analysis, there is a physical connection between L_{disk} and the behavior of the blazar SEDs. In other words, we find that the blazar sequence has a physical origin, at least for the sources studied in this work.
9. We notice that the high-redshift blazars are more Compton dominated compared to their low-redshift counterparts. However, the sample size of $z > 3$ blazars needs to be enlarged, and one should consider more BL Lac objects to make a strong claim about the evolution of blazars.

We are thankful to the journal referee for constructive comments. We are also grateful to the *Fermi*-LAT Collaboration internal referee Rodrigo Nemmen for useful suggestions and Philippe Bruel, Elizabetta Cavazzutti, Sara Cutini, Seth

Digel, Alberto Domínguez, Marcello Giroletti, and Dave Thompson for critical reading of the manuscript. The *Fermi* LAT Collaboration acknowledges generous ongoing support from a number of agencies and institutes that have supported both the development and the operation of the LAT as well as scientific data analysis. These include the National Aeronautics and Space Administration and the Department of Energy in the United States, the Commissariat à l’Energie Atomique and the Centre National de la Recherche Scientifique / Institut National de Physique Nucléaire et de Physique des Particules in France, the Agenzia Spaziale Italiana and the Istituto Nazionale di Fisica Nucleare in Italy, the Ministry of Education, Culture, Sports, Science and Technology (MEXT), High Energy Accelerator Research Organization (KEK) and Japan Aerospace Exploration Agency (JAXA) in Japan, and the K. A. Wallenberg Foundation, the Swedish Research Council and the Swedish National Space Board in Sweden. Additional support for science analysis during the operations phase is gratefully acknowledged from the Istituto Nazionale di Astrofisica in Italy and the Centre National d’Études Spatiales in France. This work performed in part under DOE Contract DE-AC02-76SF00515.

This research has made use of data obtained through the High Energy Astrophysics Science Archive Research Center Online Service, provided by the NASA/Goddard Space Flight Center. Part of this work is based on archival data, software or online services provided by the ASI Data Center (ASDC). This research has made use of the XRT Data Analysis Software (XRTDAS).

This work is based on observations obtained with XMM-Newton, an ESA science mission with instruments and contributions directly funded by ESA Member States and NASA. The scientific results reported in this article are based on data obtained from the Chandra Data Archive. This research has made use of software provided by the Chandra X-ray Center (CXC) in the application packages CIAO, ChIPS, and Sherpa.

This publication makes use of data products from the Wide-field Infrared Survey Explorer, which is a joint project of the University of California, Los Angeles, and the Jet Propulsion Laboratory/California Institute of Technology, funded by the National Aeronautics and Space Administration.

Software: SAS (v15.0.0), fermiPy (Wood et al. 2017), XSPEC (Arnaud 1996), Swift-XRT data product generator (Evans et al. 2009), CIAO (v.4.9).

REFERENCES

- Abdo, A. A., Ackermann, M., Ajello, M., et al. 2009, *ApJS*, 183, 46
- . 2010, *ApJ*, 715, 429
- . 2011, *ApJ*, 736, 131
- Abeysekara, A. U., Archambault, S., Archer, A., et al. 2015, *ApJL*, 815, L22
- Acero, F., Ackermann, M., Ajello, M., et al. 2015, *ApJS*, 218, 23
- . 2016, *ApJS*, 223, 26

- Ackermann, M., Ajello, M., Atwood, W. B., et al. 2015, *ApJ*, 810, 14
- Ackermann, M., Ajello, M., Baldini, L., et al. 2017, *ApJL*, 837, L5
- Ajello, M., Shaw, M. S., Romani, R. W., et al. 2012, *ApJ*, 751, 108
- Ajello, M., Romani, R. W., Gasparrini, D., et al. 2014, *ApJ*, 780, 73
- Ajello, M., Ghisellini, G., Paliya, V. S., et al. 2016, *ApJ*, 826, 76
- Aleksić, J., Antonelli, L. A., Antoranz, P., et al. 2011, *ApJL*, 730, L8
- Arnaud, K. A. 1996, in *Astronomical Society of the Pacific Conference Series*, Vol. 101, *Astronomical Data Analysis Software and Systems V*, ed. G. H. Jacoby & J. Barnes, 17
- Atwood, W., Albert, A., Baldini, L., et al. 2013, *ArXiv e-prints*, arXiv:1303.3514
- Atwood, W. B., Abdo, A. A., Ackermann, M., et al. 2009, *ApJ*, 697, 1071
- Bachev, R., Semkov, E., Strigachev, A., et al. 2012, *MNRAS*, 424, 2625
- Barthelmy, S. D., Barbier, L. M., Cummings, J. R., et al. 2005, *SSRv*, 120, 143
- Baumgartner, W. H., Tueller, J., Markwardt, C. B., et al. 2013, *ApJS*, 207, 19
- Begelman, M. C., & Sikora, M. 1987, *ApJ*, 322, 650
- Błażejowski, M., Sikora, M., Moderski, R., & Madejski, G. M. 2000, *ApJ*, 545, 107
- Böttcher, M., & Dermer, C. D. 2002, *ApJ*, 564, 86
- Breeveld, A. A., Landsman, W., Holland, S. T., et al. 2011, in *American Institute of Physics Conference Series*, Vol. 1358, *American Institute of Physics Conference Series*, ed. J. E. McEnery, J. L. Racusin, & N. Gehrels, 373–376
- Burrows, D. N., Hill, J. E., Nousek, J. A., et al. 2005, *SSRv*, 120, 165
- Buson, S. 2014, *The Astronomer's Telegram*, 6067, 1
- Calderone, G., Ghisellini, G., Colpi, M., & Dotti, M. 2013, *MNRAS*, 431, 210
- Cash, W. 1979, *ApJ*, 228, 939
- Castignani, G., Haardt, F., Lapi, A., et al. 2013, *A&A*, 560, A28
- Cavaliere, A., & D'Elia, V. 2002, *ApJ*, 571, 226
- Celotti, A., & Ghisellini, G. 2008, *MNRAS*, 385, 283
- Celotti, A., Padovani, P., & Ghisellini, G. 1997, *MNRAS*, 286, 415
- Chen, Y.-Y., Zhang, X., Xiong, D., & Yu, X. 2015, *AJ*, 150, 8
- Condon, J. J., Cotton, W. D., Greisen, E. W., et al. 1998, *AJ*, 115, 1693
- D'Abrusco, R., Massaro, F., Ajello, M., et al. 2012, *ApJ*, 748, 68
- De Angelis, A., Tatischeff, V., Tavani, M., et al. 2016, *ArXiv e-prints*, arXiv:1611.02232
- Dermer, C. D. 1995, *ApJL*, 446, L63
- Dermer, C. D., Finke, J. D., Krug, H., & Böttcher, M. 2009, *ApJ*, 692, 32
- Dermer, C. D., & Schlickeiser, R. 1993, *ApJ*, 416, 458
- Evans, P. A., Beardmore, A. P., Page, K. L., et al. 2009, *MNRAS*, 397, 1177
- Falomo, R., & Treves, A. 1990, *PASP*, 102, 1120
- Fan, J. H., Yang, J. H., Liu, Y., et al. 2016, *ApJS*, 226, 20
- Finke, J. D. 2013, *ApJ*, 763, 134
- Flesch, E. W. 2015, *PASA*, 32, e010
- Fossati, G., Maraschi, L., Celotti, A., Comastri, A., & Ghisellini, G. 1998, *MNRAS*, 299, 433
- Francis, P. J., Hewett, P. C., Foltz, C. B., et al. 1991, *ApJ*, 373, 465
- Frank, J., King, A., & Raine, D. J. 2002, *Accretion Power in Astrophysics*, by Juhan Frank and Andrew King and Derek Raine, pp. 398. ISBN 0521620538. Cambridge, UK: Cambridge University Press, February 2002
- Gehrels, N., Chincarini, G., Giommi, P., et al. 2004, *ApJ*, 611, 1005
- Ghisellini, G., Celotti, A., Fossati, G., Maraschi, L., & Comastri, A. 1998, *MNRAS*, 301, 451
- Ghisellini, G., Righi, C., Costamante, L., & Tavecchio, F. 2017, *MNRAS*, 469, 255
- Ghisellini, G., & Tavecchio, F. 2009, *MNRAS*, 397, 985
- . 2015, *MNRAS*, 448, 1060
- Ghisellini, G., Tavecchio, F., Foschini, L., et al. 2010, *MNRAS*, 402, 497
- Ghisellini, G., Tavecchio, F., & Ghirlanda, G. 2009, *MNRAS*, 399, 2041
- Ghisellini, G., Tavecchio, F., Maraschi, L., Celotti, A., & Sbarrato, T. 2014, *Nature*, 515, 376
- Giommi, P., Padovani, P., Polenta, G., et al. 2012a, *MNRAS*, 420, 2899
- Giommi, P., Polenta, G., Lähteenmäki, A., et al. 2012b, *A&A*, 541, A160
- Harrison, F. A., Craig, W. W., Christensen, F. E., et al. 2013, *ApJ*, 770, 103
- Hartman, R. C., Bertsch, D. L., Bloom, S. D., et al. 1999, *ApJS*, 123, 79
- Healey, S. E., Romani, R. W., Taylor, G. B., et al. 2007, *ApJS*, 171, 61
- Healey, S. E., Romani, R. W., Cotter, G., et al. 2008, *ApJS*, 175, 97
- Janiak, M., Sikora, M., & Moderski, R. 2015, *MNRAS*, 449, 431
- Jansen, F., Lumb, D., Altieri, B., et al. 2001, *A&A*, 365, L1
- Jorstad, S. G., Marscher, A. P., Larionov, V. M., et al. 2010, *ApJ*, 715, 362
- Kalberla, P. M. W., Burton, W. B., Hartmann, D., et al. 2005, *A&A*, 440, 775
- Kang, S.-J., Chen, L., & Wu, Q. 2014, *ApJS*, 215, 5
- Kaur, A., Rau, A., Ajello, M., et al. 2017, *ApJ*, 834, 41
- Komissarov, S. S., Barkov, M. V., Vlahakis, N., & Königl, A. 2007, *MNRAS*, 380, 51
- Kozłowski, S. 2017, *ApJS*, 228, 9
- Krauß, F., Wilms, J., Kadler, M., et al. 2016, *A&A*, 591, A130
- Lister, M. L., Aller, M. F., Aller, H. D., et al. 2015, *ApJL*, 810, L9
- Madejski, G. M., Nalewajko, K., Madsen, K. K., et al. 2016, *ApJ*, 831, 142
- Mao, P., Urry, C. M., Massaro, F., et al. 2016, *ApJS*, 224, 26
- Marcha, M. J. M., Browne, I. W. A., Impey, C. D., & Smith, P. S. 1996, *MNRAS*, 281, 425
- Marchesini, E. J., Andruchow, I., Cellone, S. A., et al. 2016, *A&A*, 591, A21
- Marscher, A. P. 2014, *ApJ*, 780, 87
- Marscher, A. P., & Gear, W. K. 1985, *ApJ*, 298, 114
- Massaro, E., Maselli, A., Leto, C., et al. 2015, *Ap&SS*, 357, 75
- Massaro, F., D'Abrusco, R., Ajello, M., Grindlay, J. E., & Smith, H. A. 2011, *ApJL*, 740, L48
- Massaro, F., D'Abrusco, R., Tosti, G., et al. 2012, *ApJ*, 750, 138
- McKinney, J. C., Tchekhovskoy, A., & Blandford, R. D. 2012, *MNRAS*, 423, 3083
- Meyer, E. T., Fossati, G., Georganopoulos, M., & Lister, M. L. 2011, *ApJ*, 740, 98
- Mücke, A., Engel, R., Rachen, J. P., Protheroe, R. J., & Stanev, T. 2000, *Computer Physics Communications*, 124, 290
- Nalewajko, K., Sikora, M., & Begelman, M. C. 2014, *ApJL*, 796, L5
- Narayan, R., & Piran, T. 2012, *MNRAS*, 420, 604
- Nolan, P. L., Abdo, A. A., Ackermann, M., et al. 2012, *ApJS*, 199, 31
- Odell, S. L. 1981, *ApJL*, 243, L147
- Padovani, P. 1992, *A&A*, 256, 399
- Paliya, V. S., Böttcher, M., Diltz, C., et al. 2015, *ApJ*, 811, 143
- Paliya, V. S., Parker, M. L., Fabian, A. C., & Stalin, C. S. 2016, *ApJ*, 825, 74
- Paliya, V. S., Stalin, C. S., Shukla, A., & Sahayanathan, S. 2013, *ApJ*, 768, 52
- Pjanka, P., Zdziarski, A. A., & Sikora, M. 2017, *MNRAS*, 465, 3506
- Planck Collaboration, Ade, P. A. R., Aghanim, N., et al. 2016, *A&A*, 594, A13
- Pushkarev, A. B., Kovalev, Y. Y., Lister, M. L., & Savolainen, T. 2009, *A&A*, 507, L33
- Rawlings, S., & Saunders, R. 1991, *Nature*, 349, 138
- Romani, R. W., Sowards-Emmerd, D., Greenhill, L., & Michelson, P. 2004, *ApJL*, 610, L9
- Roming, P. W. A., Kennedy, T. E., Mason, K. O., et al. 2005, *SSRv*, 120, 95
- Sagar, R., Stalin, C. S., Gopal-Krishna, & Wiita, P. J. 2004, *MNRAS*, 348, 176
- Sahayanathan, S., & Godambe, S. 2012, *MNRAS*, 419, 1660
- Savolainen, T., Homan, D. C., Hovatta, T., et al. 2010, *A&A*, 512, A24
- Sbarrato, T., Ghisellini, G., Maraschi, L., & Colpi, M. 2012, *MNRAS*, 421, 1764
- Sbarrato, T., Tagliaferri, G., Ghisellini, G., et al. 2013, *ApJ*, 777, 147
- Schlafly, E. F., & Finkbeiner, D. P. 2011, *ApJ*, 737, 103
- Shakura, N. I., & Sunyaev, R. A. 1973, *A&A*, 24, 337
- Shaw, M. S., Romani, R. W., Cotter, G., et al. 2012, *ApJ*, 748, 49
- Shen, Y., Richards, G. T., Strauss, M. A., et al. 2011, *ApJS*, 194, 45
- Sikora, M., Begelman, M. C., & Rees, M. J. 1994, *ApJ*, 421, 153
- Sikora, M., & Madejski, G. 2000, *ApJ*, 534, 109
- Sikora, M., Rutkowski, M., & Begelman, M. C. 2016, *MNRAS*, 457, 1352

- Sikora, M., Stawarz, Ł., Moderski, R., Nalewajko, K., & Madejski, G. M. 2009, *ApJ*, 704, 38
- Stalin, C. S., Gopal-Krishna, Sagar, R., & Wiita, P. J. 2002, *Bulletin of the Astronomical Society of India*, 30, 765
- Tavecchio, F., Ghisellini, G., Ghirlanda, G., Foschini, L., & Maraschi, L. 2010, *MNRAS*, 401, 1570
- Tavecchio, F., Maraschi, L., & Ghisellini, G. 1998, *ApJ*, 509, 608
- Tchekhovskoy, A., Narayan, R., & McKinney, J. C. 2011, *MNRAS*, 418, L79
- Thompson, D. J., Bertsch, D. L., Fichtel, C. E., et al. 1993, *ApJS*, 86, 629
- Thorne, K. S. 1974, *ApJ*, 191, 507
- Torrealba, J., Chavushyan, V., Cruz-González, I., et al. 2012, *RMxAA*, 48, 9
- Urry, C. M., & Padovani, P. 1995, *PASP*, 107, 803
- Vestergaard, M., & Peterson, B. M. 2006, *ApJ*, 641, 689
- Vlahakis, N., & Königl, A. 2004, *ApJ*, 605, 656
- Weisskopf, M. C., Tananbaum, H. D., Van Speybroeck, L. P., & O'Dell, S. L. 2000, in *Proc. SPIE*, Vol. 4012, X-Ray Optics, Instruments, and Missions III, ed. J. E. Truemper & B. Aschenbach, 2–16
- Wood, M., Caputo, R., Charles, E., et al. 2017, *ArXiv e-prints*, arXiv:1707.09551
- Wright, E. L., Eisenhardt, P. R. M., Mainzer, A. K., et al. 2010, *AJ*, 140, 1868
- Yan, D., Zeng, H., & Zhang, L. 2014, *MNRAS*, 439, 2933
- Yuan, W., Zhou, H. Y., Komossa, S., et al. 2008, *ApJ*, 685, 801
- Zdziarski, A. A., Sikora, M., Pjanka, P., & Tchekhovskoy, A. 2015, *MNRAS*, 451, 927
- Zhang, J., Sun, X.-N., Liang, E.-W., et al. 2014, *ApJ*, 788, 104

Table 2. The results of the spectral analysis of the *Swift*-XRT data for the γ -ray loud blazars.

Name	N_{H}	Exp.	F_{X}	$F_{\text{X, low}}$	$F_{\text{X, high}}$	Γ_{X}	$\Gamma_{\text{X, low}}$	$\Gamma_{\text{X, high}}$
[1]	[2]	[3]	[4]	[5]	[6]	[7]	[8]	[9]
J0004–4736	1.34	5.62	0.43	0.31	0.57	1.88	1.54	2.23
J0005+3820	6.57	20.31	1.91	1.30	2.10	0.03	0.00	0.36
J0011+0057	2.67	10.53	0.16	0.10	0.26	1.43	0.86	2.00
J0016–0015	2.72	3.95	0.59	0.41	1.03	1.29	0.85	1.72
J0017–0512	2.81	11.24	2.04	1.88	2.27	1.84	1.73	1.96

β_{X}	$\beta_{\text{X, low}}$	$\beta_{\text{X, high}}$	$\chi^2/\text{C-stat.}$	dof	$P_{\text{f-test}}$	Model	fit
[10]	[11]	[12]	[13]	[14]	[15]	[16]	[17]
—	—	—	26.26	48	—	PL	c-stat
1.57	1.12	1.77	25.33	30	–6.90	LP	chi
—	—	—	21.12	25	—	PL	c-stat
—	—	—	28.15	32	—	PL	c-stat
—	—	—	31.38	26	–0.22	PL	chi

NOTE—The column contents are as follows. Col.[1]: name of the CGRaBS object; Col.[2]: the Galactic neutral Hydrogen column density, in 10^{20} cm^{-2} (Kalberla et al. 2005); Col.[3]: net exposure, in ksec; Col.[4], [5], and [6]: observed 0.3–10 keV flux and its lower and upper limits, respectively, in units of $10^{-12} \text{ erg cm}^{-2} \text{ s}^{-1}$; Col.[7], [8], and [9]: power-law photon index (or spectral slope of the log parabola model at the pivot energy) and its lower and upper limits, respectively; Col.[10], [11], and [12]: the curvature parameter of the log parabola model and its lower and upper limits, respectively; Col.[13]: the statistics of the model fitting; Col.[14]: degrees of freedom; Col.[15]: log of the probability of null hypothesis derived from the f-test ; Col.[16]: the best fitted model, PL: power law, LP: log parabola; and Col.[17]: adopted statistics, c-stat: C-statistics (Cash 1979), and chi: χ^2 fitting.

(This table is available in its entirety in a machine-readable form in the online journal. A portion is shown here for guidance regarding its form and content.)

Table 3. The results of the the *Swift*-XRT data analysis for γ -ray quiet blazars.

Name	N_{H}	Exp.	F_{X}	$F_{\text{X, low}}$	$F_{\text{X, high}}$	Γ_{X}	$\Gamma_{\text{X, low}}$	$\Gamma_{\text{X, high}}$
[1]	[2]	[3]	[4]	[5]	[6]	[7]	[8]	[9]
J0001+1914	3.19	5.47	0.09	0.00	0.18	1.37	0.23	2.74
J0004+2019	3.78	1.92	0.49	0.29	0.91	1.54	0.85	2.23
J0004+4615	8.41	3.74	0.27	0.12	0.57	1.12	0.18	2.04
J0006–0623	3.22	16.38	1.80	1.67	2.00	1.67	1.56	1.77
J0008–2339	2.31	4.96	0.37	0.28	0.52	1.73	1.31	2.16

β_{X}	$\beta_{\text{X, low}}$	$\beta_{\text{X, high}}$	$\chi^2/\text{C-stat.}$	dof	$P_{\text{f-test}}$	Model	fit
[10]	[11]	[12]	[13]	[14]	[15]	[16]	[17]
—	—	—	7.53	6	—	PL	c-stat
—	—	—	15.66	15	—	PL	c-stat
—	—	—	15.50	11	—	PL	c-stat
—	—	—	22.27	28	–0.06	PL	chi
—	—	—	37.00	33	—	PL	c-stat

NOTE—The column contents are same as in Table 2.

(This table is available in its entirety in a machine-readable form in the online journal. A portion is shown here for guidance regarding its form and content.)

Table 4. *Chandra* and/or *XMM-Newton* data analysis.

Name	N_{H}	Exp.	F_{X}	$F_{\text{X, low}}$	$F_{\text{X, high}}$	Γ_{X}	$\Gamma_{\text{X, low}}$	$\Gamma_{\text{X, high}}$	$\chi^2/\text{C-stat.}$	dof	$P_{\text{f-test}}$	fit	telescope
γ -ray loud													
J0941–1335	4.08	19.82	0.42	0.38	0.45	1.76	1.61	1.92	16.80	19	-0.13	chi	Chandra
J1311+5513	1.68	3.86	0.32	0.27	0.36	1.79	1.65	1.93	21.83	20	-0.12	chi	XMM
γ -ray quiet													
J0148+3854	4.79	63.40	0.31	0.28	0.33	1.33	1.25	1.42	65.33	53	-0.33	chi	Chandra
J0254+3931	7.58	8.79	1.63	1.56	1.74	1.70	1.63	1.78	51.35	61	-0.25	chi	Chandra
J0256–3315	2.43	2.44	0.21	0.14	0.32	1.38	1.01	1.75	39.71	45	—	c-stat	Chandra
J0324–2918	1.38	3.81	0.16	0.12	0.23	1.60	1.28	1.93	50.64	51	—	c-stat	Chandra
J0439+0520	8.92	19.87	0.76	0.72	0.79	2.20	2.11	2.29	77.67	52	-0.85	chi	Chandra
J0730+4049	6.21	19.81	0.18	0.15	0.20	1.36	1.18	1.55	109.72	150	—	c-stat	Chandra
J0825+6157	3.82	18.95	1.50	1.43	1.58	1.50	1.44	1.56	88.78	80	-0.41	chi	Chandra
J0939+4141	1.16	7.09	0.30	0.26	0.35	1.70	1.52	1.90	5.55	10	-0.36	chi	Chandra
J1058+1951	1.69	149.90	2.29	2.27	2.33	1.65	1.63	1.66	478.85	346	-2.13	chi	Chandra
J1110+4403	1.30	8.45	0.21	0.18	0.25	1.35	1.19	1.51	22.30	26	-0.97	chi	XMM
J1146–2447	4.61	4.96	0.41	0.35	0.48	1.58	1.41	1.75	129.61	128	—	c-stat	Chandra
J1430+3649	1.04	3.93	0.32	0.27	0.38	1.70	1.49	1.91	79.56	95	—	c-stat	Chandra
J1431+3952	1.09	2.86	1.79	1.64	1.99	1.57	1.46	1.69	209.18	207	—	c-stat	Chandra
J1727+5510	2.72	34.61	0.60	0.57	0.65	1.58	1.48	1.67	46.50	49	-0.15	chi	Chandra
J2003–3251	7.13	13.21	0.78	0.75	0.82	1.67	1.62	1.72	121.93	141	-0.17	chi	XMM
J2354–1513	2.53	16.13	1.12	1.08	1.16	1.54	1.50	1.57	207.26	211	-0.16	chi	XMM

NOTE—The symbols have their usual meanings as given in Table 2. The last column refers to the name of the telescope from which the X-ray measurement has been taken. It should be noted that an absorbed power-law model is preferable for all sources.

Table 5. The SED parameters associated with the modeling of the broadband emission in the γ -ray loud blazars.

Name	z	θ_{v}	M_{BH}	Type	L_{disk}	R_{diss}	R_{BLR}	δ	Γ	B	p	q	γ_{min}	γ_{b}	γ_{max}	U_{e}	CD
[1]	[2]	[3]	[4]	[5]	[6]	[7]	[8]	[9]	[10]	[11]	[12]	[13]	[14]	[15]	[16]	[17]	[18]
J0004–4736	0.88	3.0	8.00	O	45.11	0.027	0.037	15.7	10	6.4	1.6	3.9	3	115	3000	-1.02	1.6
J0005+3820	0.23	3.0	8.70	E	43.76	0.033	0.008	18.6	15	0.4	2.2	3.8	9	543	5000	-1.19	7.2
J0011+0057	1.49	3.0	8.78	D	45.48	0.037	0.056	16.5	11	1.6	1.8	3.8	1	100	3000	-1.10	30.9
J0016–0015	1.58	3.0	8.87	O	45.93	0.064	0.094	17.2	12	2.2	1.8	4.4	1	120	3000	-1.29	20.3
J0017–0512	0.23	3.0	7.90	D	44.79	0.004	0.025	15.7	10	4.0	1.6	4.2	10	83	2000	0.51	4.8

NOTE—The column contents are as follows: Col.[1] and [2]: name and redshift of the source; Col.[3]: viewing angle, in degrees; Col.[4]: log scale black hole mass, in solar mass units; Col.[5]: adopted method to derive M_{BH} and L_{disk} , A: assumed; D: disk fitting, E: empirical relation, O: optical spectroscopy, and N: not used (see Table 9); Col.[6]: log scale accretion disk luminosity, in erg s^{-1} ; Col.[7]: dissipation distance, in parsec; Col.[8]: size of the BLR, in parsec; Col.[9] and [10]: the Doppler factor and the bulk Lorentz factor, respectively; Col.[11]: magnetic field strength, in Gauss; Col.[12] and [13]: spectral slopes of the broken power-law electron distribution before and after the break energy (γ_{b}), respectively; Col.[14], [15], and [16]: the minimum, break, and the maximum Lorentz factors of the emitting electron distribution; Col.[17]: the log scale particle energy density, in erg cm^{-3} ; and Col.[18]: Compton dominance.

(This table is available in its entirety in a machine-readable form in the online journal. A portion is shown here for guidance regarding its form and content.)

Table 6. The SED parameters associated with the modeling of the broadband emission in the γ -ray quiet blazars.

Name	z	θ_v	M_{BH}	Type	L_{disk}	R_{diss}	R_{BLR}	δ	Γ	B	p	q	γ_{min}	γ_b	γ_{max}	U_e	CD
[1]	[2]	[3]	[4]	[5]	[6]	[7]	[8]	[9]	[10]	[11]	[12]	[13]	[14]	[15]	[16]	[17]	[18]
J0001+1914	3.10	3.0	8.70	A	45.00	0.038	0.032	17.2	12	2.7	2.0	3.6	2	177	4000	-0.83	2.5
J0004+2019	0.68	3.0	8.70	A	44.00	0.012	0.010	14.8	9	2.5	2.1	3.6	1	38	4000	0.51	2.4
J0004+4615	1.81	3.0	8.70	A	45.00	0.041	0.032	16.5	11	2.1	1.9	3.6	2	53	4000	-0.56	2.2
J0006-0623	0.35	3.0	8.70	A	44.00	0.029	0.010	14.7	9	1.5	1.7	3.8	20	467	3000	-1.00	0.2
J0008-2339	1.41	3.0	9.30	D	47.00	0.880	0.323	15.7	10	0.2	1.6	3.8	1	234	3000	-3.00	13.0

NOTE—The column contents are same as in Table 5.

(This table is available in its entirety in a machine-readable form in the online journal. A portion is shown here for guidance regarding its form and content.)

Table 7. The jet powers derived from the modeling of the broadband emission in the γ -ray loud blazars.

Name	P_{ele}	P_{mag}	P_{rad}	P_{kin}	P_{jet}
[1]	[2]	[3]	[4]	[5]	[6]
J0004-4736	44.09	45.32	45.65	46.09	46.17
J0005+3820	44.45	43.45	44.39	46.24	46.25
J0011+0057	44.38	44.49	45.45	46.84	46.84
J0016-0015	44.73	45.31	46.12	47.16	47.17
J0017-0512	44.01	43.31	44.39	45.78	45.79

NOTE—The column contents are as follows: Col.[1] name the source; Col.[2], [3], [4], [5], and [6]: the electron, magnetic, radiative, kinetic, and total jet power, respectively. Note that $P_{\text{jet}} = P_{\text{ele}} + P_{\text{mag}} + P_{\text{kin}}$. All jet powers are evaluated for a two-sided jet.

(This table is available in its entirety in a machine-readable form in the online journal. A portion is shown here for guidance regarding its form and content.)

Table 8. The jet powers derived from the modeling of the broadband emission in γ -ray quiet blazars.

Name	P_{ele}	P_{mag}	P_{rad}	P_{kin}	P_{jet}
[1]	[2]	[3]	[4]	[5]	[6]
J0001+1914	44.75	45.04	45.80	47.05	47.05
J0004+2019	44.84	43.72	44.48	47.57	47.57
J0004+4615	45.00	44.80	45.39	47.37	47.37
J0006-0623	44.07	44.03	45.02	45.39	45.42
J0008-2339	44.47	45.34	45.20	46.67	46.70

NOTE—The column contents are same as in Table 7.

(This table is available in its entirety in a machine-readable form in the online journal. A portion is shown here for guidance regarding its form and content.)

Table 9. The list of 13 γ -ray loud blazars which are modeled with synchrotron and SSC processes, i.e., without invoking EC mechanism.

Name	z
J1015+4926	0.21
J1104+3812	0.03
J1136+7009	0.04
J1217+3007	0.13
J1230+2518	0.14
J1555+1111	0.36
J1653+3945	0.03
J1725+1152	0.02
J1728+5013	0.06
J1917–1921	0.14
J1959+6508	0.05
J2009–4849	0.07
J2158–3013	0.12

Table 10. Results of the correlation analysis, by means of a Monte Carlo simulation, performed on the sample of the γ -ray loud and the γ -ray quiet blazars.

	N	ρ_s	PNC	ρ_{par}	PNC
P_{rad} vs. L_{disk}					
γ -ray loud	311	0.66 ± 0.04	$< 1 \times 10^{-5}$	0.22 ± 0.10	$< 1 \times 10^{-5}$
γ -ray quiet	191	0.67 ± 0.05	$< 1 \times 10^{-5}$	0.29 ± 0.20	$< 1 \times 10^{-5}$
All sources	502	0.63 ± 0.03	$< 1 \times 10^{-5}$	0.19 ± 0.08	$< 1 \times 10^{-5}$
P_{jet} vs. $\dot{M}c^2$					
γ -ray loud	311	0.67 ± 0.04	$< 1 \times 10^{-5}$	0.53 ± 0.08	$< 1 \times 10^{-5}$
γ -ray quiet	191	0.21 ± 0.08	5.0×10^{-2}	0.02 ± 0.13	6.5×10^{-1}
All sources	502	0.67 ± 0.03	$< 1 \times 10^{-5}$	0.56 ± 0.06	$< 1 \times 10^{-5}$
M_{BH} vs. z					
γ -ray loud	228	0.47 ± 0.06	$< 1 \times 10^{-5}$	—	—
γ -ray quiet	181	0.46 ± 0.06	$< 1 \times 10^{-5}$	—	—
All sources	409	0.50 ± 0.04	$< 1 \times 10^{-5}$	—	—
L_{disk} vs. M_{BH}					
γ -ray loud	228	0.51 ± 0.07	$< 1 \times 10^{-5}$	0.45 ± 0.08	$< 1 \times 10^{-5}$
γ -ray quiet	181	0.43 ± 0.08	1.8×10^{-4}	0.59 ± 0.11	$< 1 \times 10^{-5}$
All sources	409	0.42 ± 0.05	$< 1 \times 10^{-5}$	0.39 ± 0.06	$< 1 \times 10^{-5}$
P_{jet} vs. M_{BH}					
γ -ray loud	228	0.29 ± 0.07	3.2×10^{-3}	0.22 ± 0.11	1×10^{-4}
γ -ray quiet	181	-0.02 ± 0.08	4.7×10^{-1}	-0.23 ± 0.11	3×10^{-1}
All sources	409	0.26 ± 0.05	4.9×10^{-4}	0.17 ± 0.09	5×10^{-4}
CD vs. M_{BH}					
γ -ray loud	228	0.33 ± 0.07	5.7×10^{-4}	0.01 ± 0.10	8.7×10^{-1}
γ -ray quiet	181	0.45 ± 0.08	1.3×10^{-4}	0.18 ± 0.10	1.3×10^{-2}
All sources	409	0.30 ± 0.05	$< 1 \times 10^{-5}$	0.00 ± 0.09	7.3×10^{-1}
$L_{\text{disk}}/L_{\text{Edd}}$ vs. γ_b					
γ -ray loud	311	-0.33 ± 0.06	4.4×10^{-5}	—	—
γ -ray quiet	191	-0.28 ± 0.08	7.4×10^{-3}	—	—
All sources	502	-0.30 ± 0.05	$< 1 \times 10^{-5}$	—	—
$L_{\text{disk}}/L_{\text{Edd}}$ vs. R_{diss}					
γ -ray loud	311	-0.60 ± 0.04	$< 1 \times 10^{-5}$	—	—
γ -ray quiet	191	-0.64 ± 0.05	$< 1 \times 10^{-5}$	—	—
All sources	502	-0.64 ± 0.03	$< 1 \times 10^{-5}$	—	—
CD vs. L_{disk}					
γ -ray loud	311	0.61 ± 0.04	$< 1 \times 10^{-5}$	0.36 ± 0.08	$< 1 \times 10^{-5}$
γ -ray quiet	191	0.61 ± 0.05	$< 1 \times 10^{-5}$	0.42 ± 0.08	$< 1 \times 10^{-5}$
All sources	502	0.51 ± 0.04	$< 1 \times 10^{-5}$	0.31 ± 0.07	$< 1 \times 10^{-5}$
CD vs. P_{jet}					
γ -ray loud	324	0.50 ± 0.05	$< 1 \times 10^{-5}$	0.22 ± 0.07	$< 1 \times 10^{-5}$
γ -ray quiet	191	-0.02 ± 0.07	4.7×10^{-1}	-0.20 ± 0.09	3×10^{-3}

Table 10 continued

Table 10 (*continued*)

	N	ρ_s	PNC	ρ_{par}	PNC
All sources	515	0.32 ± 0.05	$< 1 \times 10^{-5}$	0.09 ± 0.06	6.7×10^{-3}
<i>L_{disk} vs. z</i>					
γ -ray loud	311	0.70 ± 0.03	$< 1 \times 10^{-5}$	—	—
γ -ray quiet	191	0.73 ± 0.04	$< 1 \times 10^{-5}$	—	—
All sources	502	0.74 ± 0.02	$< 1 \times 10^{-5}$	—	—
<i>P_{jet} vs. z</i>					
γ -ray loud	324	0.50 ± 0.05	$< 1 \times 10^{-5}$	—	—
γ -ray quiet	191	0.45 ± 0.06	$< 1 \times 10^{-5}$	—	—
All sources	515	0.49 ± 0.04	$< 1 \times 10^{-5}$	—	—
<i>CD vs. z</i>					
γ -ray loud	324	0.53 ± 0.05	$< 1 \times 10^{-5}$	—	—
γ -ray quiet	191	0.32 ± 0.07	1.2×10^{-3}	—	—
All sources	515	0.54 ± 0.04	$< 1 \times 10^{-5}$	—	—

NOTE—N denotes the number of sources. Whenever applicable, we also provide the results associated with the partial correlation analysis. ρ_s and ρ_{par} correspond to Spearman’s rank-correlation coefficients for a simple correlation and partial correlation test, respectively. The associated probabilities of no correlation are also given. We perform a semi-partial correlation test when one of the parameters is Compton dominance, a redshift-independent quantity. See the text for details.